

# Flutter in Functionally Graded Conical Shell under Follower Force

Rupsagar Chatterjee<sup>1</sup>, Sudib Kumar Mishra<sup>2</sup>

1 - Associate Engineer, Airbus Group India Private Limited, Bangalore, India

2 - Professor, Department of Civil Engineering, Indian Institute of Technology Kanpur, UP, India

**ABSTRACT:** Truncated conical shells are essential components of rocket booster nozzles and thrust vector control (TVC) systems for the propulsion of multi-stage launch vehicles. The TVCs assist the ascent of launch vehicles by directing the resultant thrust from the boosters, acting as a follower force that might trigger instability. Previous studies on instability of aerospace structures are mostly limited to beams, plates and cylindrical shells. This study analyses a truncated conical shell under a follower force of constant magnitude, considering thickness-wise gradation of material properties employed for thermal management. The governing equations are derived following Hamilton's principle, considering first-order shear deformation theory and, solved using finite element method. Clamped and free boundaries are assumed at the small and large ends. The influence of mass and stiffness proportional damping is considered. Although strong flutter appears as the dominant instability mode, instances of erratic weak instabilities are also observed for undamped and lightly damped cases. Damping enhances stability but its effect gets saturated. The flutter loads are presented for varying non-dimensional parameters, characterizing the shell geometry and material properties.

**Keywords:** Truncated conical shell, Functionally graded material, First-order shear deformation, Flutter instability, Non-conservative follower force, Proportional damping.

**Correspondence to:** Sudib Kumar Mishra; **E-mail:** [smishra@iitk.ac.in](mailto:smishra@iitk.ac.in)

## 1. Introduction

Shells are widely used in engineering because of their efficient load-carrying behavior, high strength-to-weight ratio, and ability to contain space by their geometry. Shells find wide applications as storage structures, containment for nuclear power plants, domes, pressure vessels, aircraft propulsion systems, fuselages, rockets, missiles, ships, and submarines. Many biological lifeforms like plants, animals, and human organs (eyes, skull, bones, and joints) are inherently shell structures.

Functionally graded materials (FGMs) are an advanced class of inhomogeneous composite materials. But unlike conventional composites, the mechanical, thermal, and chemical properties of FGMs can vary smoothly across thickness. Because of this, no material interface appears, although the resulting FGM inherits its constituents' properties. The gradual change of properties alleviates several difficulties associated with conventional materials. It improves the bond strength by eliminating any stress singularity that can otherwise be present in composites. Moreover, FGMs can reduce residual stresses in high thermal gradient environments due to the gradually changing thermal expansion coefficient. FGMs have found widespread applications as super heat-resistant refractory materials in spacecraft, nuclear reactors, high-efficiency energy conversion materials, biomaterials, and optical and electronic components [1,2]. Functionally graded shells have gained prominence in recent years as a viable structural material for launch vehicles, owing to the feasibility of creating thermal barriers in structures exposed to high-temperature gradients [3].

Depending on the functional gradation of material properties, FGMs can be of three types: power-law (P), exponential (E), and sigmoid (S). PFGM and EFGM are the most commonly used descriptions of FGM where the constituent materials vary as per power-law and exponential functions, respectively [4]. However, in both these FGM, stress concentration occurs at one of the interfaces where the material composition varies rapidly. To eliminate this, a sigmoid variation can be introduced, where the volume fraction is defined using two power-law functions. SFGMs have been shown to reduce the stress intensity factor and arrest crack growth in cracked specimens [5].

Over the past century, researchers have put forward various theories of shells. Many of these works are commonly referred to as classical shell theories, in which the Kirchhoff-Love hypothesis with thin shell assumptions approximates the displacement fields. Contrary to the theories of thin shells, thick shell theories consider the effect of transverse shear deformations and rotary inertia. The rotations of the normal to the surface are considered in addition to the displacement components [6].

While the vibration and stability characteristics of plates and cylindrical shells have long been extensively researched, it is only recently that such investigation into conical shells have gained prominence [7]. Early works on truncated conical shells mainly dealt with free vibration analysis using different analytical and numerical techniques by adopting isotropic or laminated composite materials [8–14]. Recent studies in advanced numerical simulations of plates and shells incorporate alternate choices of materials, including but not limited to functionally graded (FG) or carbon nanotube (CNT) reinforced nanocomposites, owing to

their widespread applications. The free vibration and thermo-elastic buckling analyses of laminated composite and FG truncated conical shells have been studied using first-order shear deformation theory (FSDT) in many literatures [15–18]. Malekzadeh et al. [19] studied the three-dimensional free vibration of FGM truncated conical shells subjected to thermal environment using the differential quadrature method (DQM). Nejati et al. [20] presented a parametric study of free vibration of CNT-reinforced FG truncated conical shell using generalized differential quadrature (GDQ) and third-order shear deformation theory (TSDT). Zghal et al. [21] analyzed the free vibration of CNT-reinforced FG composite shells for different distributions of CNT. The material properties were derived using micro-mechanical model with efficiency parameters. Sofiyev [22] showed the vibration and stability characteristics of axially loaded heterogeneous CNT-reinforced truncated conical shell. Song et al. [23] investigated the free vibration characteristics of truncated conical shells with non-classical boundary conditions having elastic constraints and added mass. Fares et al. [24] showed the free vibration analysis of CNT-reinforced multilayered FG truncated conical shell with mixed mode formulation. Li et al. [25] analyzed the free vibration of porous metal foam truncated conical shell under elastic boundary conditions considering FSDT and different porosity distributions. Zghal et al. [26] determined the thermal free vibration characteristics of FGM plates and shells using an improved FSDT shell model. Avramov et al. [27] showed how ring stiffener reduces the amplitude of transient response of CNT-reinforced FG conical shell using higher-order shear deformation theory (HSDT). Wang et al. [28] presented the free vibration analysis of a spinning FG spherical-cylindrical-conical shell with arbitrary boundary conditions in a thermal environment. Vescovini and Fantuzzi [29] analyzed the free vibration of conical shells using the Ritz method with arbitrary boundary conditions. Sofiyev and others [30,31] have put forward analytical methods for stability analysis of FG CNT-reinforced and heterogeneous orthotropic conical shells under external pressure using FSDT. Pakpia et al. [32] proposed an analytical model of stability behavior of corrugated conical shell having orthotropy with FSDT. Yang et al. [33] studied the crashworthiness of corrugated hierarchical truncated conical shells by numerical and experimental methods under axial compression.

A review of the literature shows many researchers have also investigated the nonlinear stability behavior of FG plates and shells. Sofiyev and co-authors [34–41] have extensively studied the nonlinear vibration of FG truncated conical shell. Some of their works have assumed shell model supported on elastic foundation with large deformation theory and von Karman-Donnell type kinematic nonlinearity. Zghal et al. [42] showed the buckling

analysis of power-law based FG and FG-CNT-reinforced plates and curved panels employing higher order shell model in nonlinear finite element framework. Trabelsi et al. [43,44] investigated the thermal buckling and post-buckling of FG plates and cylindrical shells using modified FSDT. Trabelsi et al. [45] also investigated the thermal buckling and post-buckling response of FG plates and shells using a geometrically nonlinear Kirchhoff shell model. Allahkarami et al. [46] presented a parametric study of dynamic buckling of a bi-directional functionally graded (BD-FG) truncated conical shell on an elastic foundation with FSDT. The governing equations were derived using Hamilton's principle and solved by the GDQ method. Zarei et al. [47] studied the global buckling behavior of laminated sandwich conical shells with lattice cores for different design parameters employing FSDT and the Galerkin method. Fu et al. [48] analytically determined the dynamic instability of FG sandwich conical shells under periodic axial and lateral load. They studied the effect of sandwich types, gradient indices, skin-core-skin ratio, and load forms on the stability behavior. Zghal et al. [49] analyzed the post-buckling behavior of FG-CNT-reinforced composites. Zghal and Dammak [50] studied the vibration characteristics of porous imperfect FGM plates and shells with modified FSDT. Using SFGM gradation, Huang et al. [51] performed vibration and buckling analysis of porous truncated conical shell showing the effect of pores, ceramic mass fraction and power-law gradation with Galerkin's method. Hasan et al. [52] investigated the buckling and post-buckling behavior of temperature dependent laminated graphene-enhanced composite (GEC) truncated conical shells subjected to torsion for different geometric parameters and graphene distribution.

Lately, numerous studies have been conducted on flutter instability of functionally graded plates and shells in supersonic airflow. Ibrahim et al. [53] presented the flutter and post-buckling behavior of functionally graded rectangular plates using nonlinear finite element analysis considering thermal effects and aerodynamic pressure, using thin plate assumption. In another work, Ibrahim et al. [54] also studied the flutter phenomenon in thin rectangular FGM plates using nonlinear finite element method under the combined effect of supersonic airflow, thermal, and random acoustic loads. Mahmoudkhani et al. [55] determined the aeroelastic stability boundaries of simply supported FGM conical shells subjected to supersonic flow under a thermal environment. Sabri and Lakis [56] proposed a hybrid finite element formulation based on Sanders' thin shell theory and finite element method to predict flutter in FGM cylindrical shells under supersonic airflow. Su et al. [57] developed a unified approach for the vibration and flutter analysis of elastically restrained first-order shear deformable stiffened FGM plates. Wei et al. [58] studied the flutter behavior

of axially functionally graded (AFG) cylindrical shells. It was shown that such structures could have superior aeroelastic qualities with a judicious choice of parameters. Sun et al. [59] argued that the aeroelastic stability of systems could be improved against flutter by adding lumped masses, which may be an effective design methodology for the AFG panels. Muc and Flis [60] presented free vibration and flutter behavior for porous functionally graded rectangular plates using analytical and Rayleigh-Ritz methods. Zhou et al. [61] showed the free vibration and flutter characteristics of graphene platelet (GPL) reinforced porous FGM cylindrical panels. AminYazdi [62] performed a flutter analysis of FG-CNT-reinforced double-curved shells with geometric imperfections using homotopy perturbation. Avramov and Uspensky [63] investigated the geometrically nonlinear flutter instability of a sandwich truncated conical shell with honeycomb core under supersonic flow. The nonlinear self-sustained quasi-periodic and chaotic vibration amplitudes were shown to be larger than the amplitudes of periodic vibration for different boundary conditions. Houshang et al. [64] analyzed the supersonic flutter of a sandwich truncated conical shell with a magneto-rheological (MR) core. Banijamali and Jafari [65] recently studied the vibration characteristics of rotating FG conical shells stiffened with anisogrid lattice structure. They presented a parametric study of the travelling wave frequencies with regard to critical rotating speed. Since flutter can cause detrimental effects on structural integrity, many recent works have also focused on active and passive control methods of flutter suppression in plates and shells [66–69].

Several investigations have been reported in the literature on the stability of beams, plates, and shells under different types of follower forces [70,71]. In this context, Park and Kim [72] studied the dynamic instability of a free-free cylindrical shell with FSDT. Torki et al. [73] performed a dynamic instability analysis of cantilever FGM cylindrical shells subjected to follower force and showed the influence of gradation volume fraction and thickness on the flutter loads. In another study, Torki et al. [74] investigated the flutter of cantilever FGM cylindrical shells considering uniformly distributed and linearly increasing follower forces. Robinson and Adali [75] analyzed viscoelastic rectangular plates under distributed follower force with different boundary conditions. They showed the type of instability under follower force is strongly influenced by the boundary conditions. The dynamic behavior of beams subjected to distributed follower force are studied in [76,77] using geometrically exact nonlinear composite beam theory. Ventura et al. [78] investigated the buckling of thin pressurized cylindrical shells numerically using Asymptotic Numerical Method (ANS) under conservative and non-conservative (follower) loadings. Do et al. [79]

proposed closed-form solutions of critical follower external pressure for elasto-plastic buckling of cylindrical and spherical shells. The aeroelastic response of aircraft wings under combined bending-torsion from follower forces of mounted engines has been studied in [80–82] showing the effects of engine location and mass.

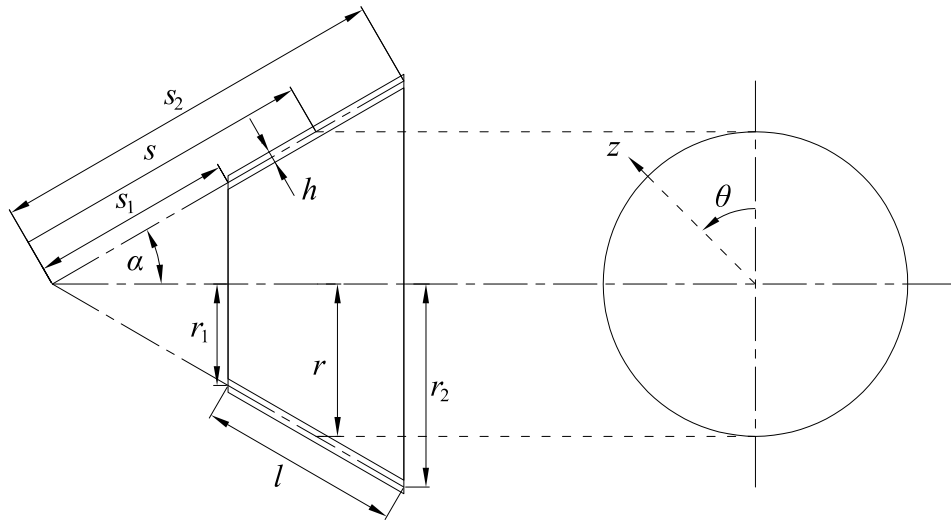
FG truncated conical shells are one of the essential structural components in the propulsion system of launch vehicles. In present-day multi-stage launch vehicles, they find extensive use as rocket booster nozzles and thrust vector control (TVC) systems. After the propellant combustion in booster engines, the nozzle extension at the rear end of the launch vehicle discharges the exhaust to generate the required thrust for lift-off and subsequent flight of the vehicle. During this operation, high pressure acts on the nozzle, causing elastic deformations in its body. These deformations change the direction of the generated thrust from the boosters. Of course, the TVCs assist in sophisticated maneuvering in the flight path during the ascent of the launch vehicle by appropriately directing the resultant thrust from the boosters. Nevertheless, a follower force acts on the nozzle. However, it is evident from the published studies that though the behavior of space launching structures has been idealized as cylindrical shells and beams under follower force in previous investigations, a lacuna exists in the study of stability characteristics of truncated conical shells subjected to follower force. The present study aims to address this research gap. This study presents the stability behavior of FG truncated conical shells subjected to follower force of constant magnitude. The governing equations of the first-order shear deformable shell is derived using Hamilton's principle and solved the using finite element method, approximating the circumferential displacements by harmonic functions. The convergence and validity of the proposed model are checked; then, some parametric studies are conducted. The study accommodates varying geometry of the shells by adjusting the semi-vertex angle, slant height, radius, and thickness. Different characteristics of the material properties (namely, the damping, functional gradation exponent, and so on) for the shell are included in the analysis to study their influences on the stability against flutter. The remainder of the article is organized as follows. Section 2 illustrates the adopted shell model with the governing equations and explains the solution methodology. Section 3 discusses the mesh sensitivity of the proposed finite element model and validates it with the existing literature. The dynamic instability characteristics of the FGM truncated conical shell are presented along with an overview of free vibration behavior. The results from the parametric studies are presented here. Section 4 summarizes the article with concluding remarks.

## 2. Formulation of the governing equations

The geometry of a truncated conical shell is shown in Fig. 1(a). In this figure,  $\alpha$  refers to the semi-vertex angle of the complete cone. The coordinate system is taken in a way, such that the  $s$  coordinate axis runs along a meridian starting from the apex of the cone to the larger base and acts as a generator of the surface. The angular coordinate  $\theta$  runs circumferentially at any section from a reference meridian. The direction normal to both  $s$  and  $\theta$  is taken to be the  $z$  direction and is positive outward from the shell middle surface. The shell is assumed to have constant thickness  $h$ . The symbol  $l$  denotes the slanted height of the frustum. The radius of midplane ( $z=0$ ) at any distance  $s$  is  $r(s) = s \sin \alpha$ .

For studying the dynamic stability, the smaller end of the conical shell is assumed to be clamped whereas the larger end is kept free. The larger end is subjected to a uniformly distributed follower force of constant intensity  $P$ , shown in Fig. 1(b). This force is assumed to be acting along the mid-surface of the shell and remains tangential to the meridian at all points on the edge at any configuration of the shell. Thus, the direction of the follower force at any two diametrically opposite points on the free edge would not be parallel due to the conical shape of the shell, which is unlike the case of a cylindrical shells, for which the meridians are parallel to the surface generator.

(a)



(b)

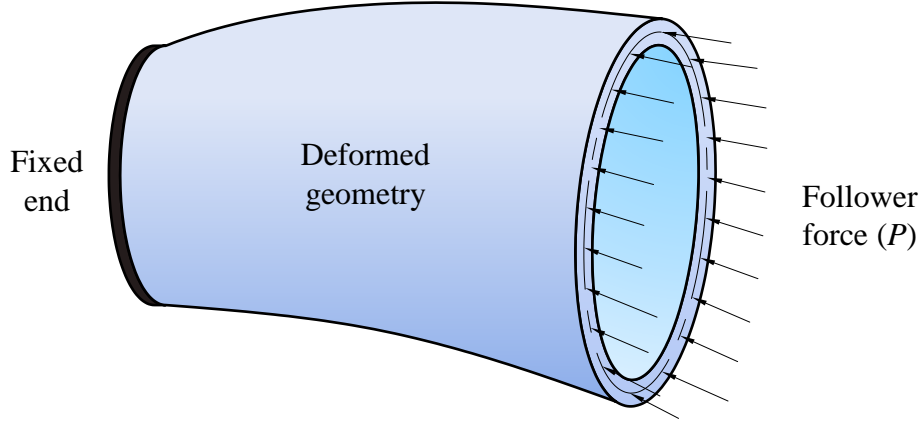


**Fig. 1.** Schematic representation of a truncated conical shell: (a) Geometry of a truncated conical shell along with the reference coordinate system; (b) A deformed truncated conical shell with clamped small end and free large end subjected to uniformly distributed follower force along the mid-surface of the larger edge.

The density, Young's modulus and Poisson's ratio for the FG shell at any depth  $z$  from the mid-surface are denoted by  $\rho$ ,  $E$  and  $\nu$  respectively. The Poisson's ratio for the FGM is reasonably assumed to be constant to avoid complexity [83]. However, the density and Young's modulus vary continuously across the thickness of the shell. As such, these quantities for the homogeneous constituent of the FGM are added with subscripts  $i$  and  $o$  (i.e.  $\rho_i$ ,  $E_i$ ,  $\rho_o$  and  $E_o$ ) to represent the properties at the inner and outer shell surfaces, respectively. In this study, two FGM models are considered for the truncated conical shell, namely, power-law type FGM (PFGM) and the exponential type FGM (EFGM) [4]. The material properties vary as a power-law function of the volume fraction of the constituents in PFGM. Depending on the surface of choice, from where the volume fraction is controlled, alternative formulations can be found in the literature [16]. In this work, the volume fraction of the inner surface constituent at any depth  $z$  is taken as  $V_i(z) = (0.5 - z/h)^\eta$ . Here,  $z/h = -0.5$  corresponds to the inner surface of the truncated conical shell. The total volume fraction of the inner and outer surface constituents at any depth within the shell is always unity. That is,  $V_i(z) + V_o(z) = 1$ , where,  $V_o$  is the volume fraction of the outer surface constituent. Using the rule of mixtures, the density and Young's modulus at any point in the PFGM becomes

$$\rho(z) = \rho_i V_i(z) + \rho_o V_o(z), \quad E(z) = E_i V_i(z) + E_o V_o(z), \quad (1)$$



where the volume fraction index  $\eta$  ( $0 \leq \eta < \infty$ ) determines the variation profile of the constituent materials. For  $\eta = 0$ , the PFGM shell is completely composed of the inner surface material whereas, for  $\eta \rightarrow \infty$ , it is entirely composed of the outer surface material. Naturally, these cases represent the special case of a shell with homogeneous material. In EFGM, the material properties between the two surfaces of a truncated conical shell vary exponentially [4] as follows

$$\rho(z) = \rho_o \exp\left(\left(\frac{1}{2} - \frac{z}{h}\right) \ln\left(\frac{\rho_i}{\rho_o}\right)\right), \quad E(z) = E_o \exp\left(\left(\frac{1}{2} - \frac{z}{h}\right) \ln\left(\frac{E_i}{E_o}\right)\right). \quad (2)$$

A moderately thick shell is considered in the present work and therefore the Reissner-Mindlin first-order shear deformation theory (FSDT) is used for analysis. Based on the assumptions of the first-order shear deformation theory, the displacement components  $(\bar{u}, \bar{v}, \bar{w})$  at any point in the shell having coordinates  $(s, \theta, z)$  at time  $t$  is written as

$$\begin{cases} \bar{u}(s, \theta, z, t) = u(s, \theta, t) + z\phi(s, \theta, t) \\ \bar{v}(s, \theta, z, t) = v(s, \theta, t) + z\psi(s, \theta, t) \\ \bar{w}(s, \theta, z, t) = w(s, \theta, t) \end{cases}, \quad (3)$$

where  $u$ ,  $v$  and  $w$  represent the displacement components of the shell middle surface in the  $s$ ,  $\theta$  and  $z$  directions respectively. The quantities  $\phi$  and  $\psi$  denote the rotations of the normal to the middle surface with respect to  $s$  and  $\theta$  directions, respectively. No shear correction factor is assumed in the analysis. The solution of the generalized displacements is assumed of the following form

$$\begin{cases} u(s, \theta, t) = \sum_{n=0}^{\infty} e^{\lambda t} \bar{U}(s) \cos n\theta, \quad v(s, \theta, t) = \sum_{n=0}^{\infty} e^{\lambda t} \bar{V}(s) \sin n\theta \\ w(s, \theta, t) = \sum_{n=0}^{\infty} e^{\lambda t} \bar{W}(s) \cos n\theta, \quad \phi(s, \theta, t) = \sum_{n=0}^{\infty} e^{\lambda t} \bar{\Phi}(s) \cos n\theta \\ \psi(s, \theta, t) = \sum_{n=0}^{\infty} e^{\lambda t} \bar{\Psi}(s) \sin n\theta \end{cases}, \quad (4)$$

where  $\bar{U}$ ,  $\bar{V}$ ,  $\bar{W}$ ,  $\bar{\Phi}$  and  $\bar{\Psi}$  are the shape functions of the respective displacement fields along the  $s$  direction and  $n$  denotes the circumferential wave number.

Applying the Hamilton's principle, the equation of motion for the truncated conical shell subjected to follower force can be written as

$$\int_{t_1}^{t_2} (\delta T - \delta U - \delta V + \delta W_{nc}) dt = 0, \quad (5)$$

where  $\delta T$ ,  $\delta U$ ,  $\delta V$  represent the variations of the kinetic energy, strain energy and potential energy due to the conservative part of the follower force, whereas  $\delta W_{nc}$  represents the virtual work done by the non-conservative part of the follower force, respectively [72,84]. Individual terms of the integrand are obtained as

$$\delta T = \int_0^{2\pi} \int_{s_1}^{s_2} \int_{-\frac{h}{2}}^{\frac{h}{2}} \rho \left\{ u_t \delta u_t + v_t \delta v_t + w_t \delta w_t + z^2 (\phi_t \delta \phi_t + \psi_t \delta \psi_t) \right\} (s \sin \alpha + z) dz ds d\theta, \quad (6)$$

$$\delta U = \int_0^{2\pi} \int_{s_1}^{s_2} \int_{-\frac{h}{2}}^{\frac{h}{2}} \boldsymbol{\epsilon}^T \mathbf{D} \delta \boldsymbol{\epsilon} (s \sin \alpha + z) dz ds d\theta \quad (7)$$

$$\delta V = P \int_0^{2\pi} \int_{s_1}^{s_2} \left( \frac{\partial w}{\partial s} \frac{\partial \delta w}{\partial s} + \frac{\partial v}{\partial s} \frac{\partial \delta v}{\partial s} \right) s \sin \alpha ds d\theta \quad (8)$$

$$\delta W_{nc} = P \int_0^{2\pi} \left[ \left( \delta w \frac{\partial w}{\partial s} + \delta v \frac{\partial v}{\partial s} \right) s \sin \alpha \right]_{s=s_2} d\theta \quad (9)$$

The strain  $\boldsymbol{\epsilon} = [\epsilon_{ss} \quad \epsilon_{\theta\theta} \quad \epsilon_{s\theta} \quad \epsilon_{sz} \quad \epsilon_{\theta z}]^T$  at any point is related to the stress  $\boldsymbol{\sigma} = [\sigma_{ss} \quad \sigma_{\theta\theta} \quad \sigma_{s\theta} \quad \sigma_{sz} \quad \sigma_{\theta z}]^T$  through  $\boldsymbol{\sigma} = \mathbf{D} \boldsymbol{\epsilon}$ , where the linear elastic isotropic constitutive matrix ( $\mathbf{D}$ ) is given by Eq. (A.1).

In order to facilitate finite element formulation of the governing equations, a three-node Lagrange element is adopted for discretization of the truncated conical shell along the  $s$  coordinate. It may be noted that the approximation along the  $\theta$  coordinate leads to a ring element in the circumferential direction of the shell. Using Eqs. (3) and (4), the expression for strain can be given as

$$\boldsymbol{\epsilon} = \boldsymbol{\Xi} \sum_{n=0}^{\infty} e^{At} \mathbf{N}(s, \theta, n) \bar{\boldsymbol{\Lambda}} = \sum_{n=0}^{\infty} e^{At} \boldsymbol{\Xi} \mathbf{N}(s, \theta, n) \bar{\boldsymbol{\Lambda}}. \quad (10)$$

where  $\bar{\boldsymbol{\Lambda}}$  is the generalized nodal displacement vector of the shell mid-surface in the discretized geometry, and  $\mathbf{N}$  is the shape function matrix. The kinematic operator  $\boldsymbol{\Xi}$  is given in Eq. (A.2). It can be seen from Eqs. (6) to (9) that the shape functions are mutually orthogonal with respect to the circumferential bases. This is true for shells with axisymmetric geometry and boundary conditions. Since the equations hold true for any arbitrary

circumferential mode, they can be solved separately for each  $n$ . Thus, the summations and the superscripts in Eq. (10) can be conveniently dropped without loss of generality. The element mass  $(\mathbf{M}^{(e)})$  and stiffness  $(\mathbf{K}^{(e)}, \mathbf{Q}_C^{(e)}, \mathbf{Q}_N^{(e)})$  matrices are obtained analytically from Eqs. (6) to (9) respectively using commercial software Maple. It can be shown that  $\mathbf{M}^{(e)}$ ,  $\mathbf{K}^{(e)}$  and  $\mathbf{Q}_C^{(e)}$  will yield symmetric matrices while  $\mathbf{Q}_N^{(e)}$  will be non-symmetric matrix. Further, it can be found that the matrices  $\mathbf{M}^{(e)}$ ,  $\mathbf{Q}_C^{(e)}$  and  $\mathbf{Q}_N^{(e)}$  are independent of the circumferential wave number  $n$  while  $\mathbf{K}^{(e)}$  is not.

Damping has been introduced in the structure as mass and stiffness proportional [85]. Taking  $\zeta$  as the identical damping ratio for the first two vibration modes,  $\mathbf{d}$  as the vector of unrestrained nodal DOFs, and evaluating Eq. (5) with correct assembly of the element matrices and boundary conditions, one obtains

$$(\Lambda^2 \mathbf{M} + \Lambda \mathbf{C} + \mathbf{K} + P(\mathbf{Q}_N - \mathbf{Q}_C)) \mathbf{d} = \mathbf{0}. \quad (11)$$

where the matrices stand for the assembled system.  $\mathbf{C} = \gamma_1 \mathbf{M} + \gamma_2 \mathbf{K}$  with  $\gamma_1, \gamma_2$  related to the first two undamped natural frequencies  $(\Omega_1, \Omega_2)$  as per Eq. (A.3). Eq. (11) can be transformed into standard linear eigenvalue problem  $\mathbf{A} \mathbf{q} = \mu \mathbf{q}$  [70] and the eigenvalues are determined from

$$\det(\mathbf{A} - \mu \mathbf{I}) = 0, \quad (12)$$

where,  $\mathbf{A}$ ,  $\mathbf{q}$ , and  $\mu$  are given in Eq. (A.4). The complex frequency  $\Lambda$  is expressed as  $\Lambda = \Theta \pm i\Omega$ , where  $\Omega \geq 0$ . The cyclic frequency of the system is  $f = \Omega / 2\pi$ . Depending upon the values of  $\Theta$  and  $\Omega$ , distinct cases may arise, as given in Table B.1. With the addition of follower force, the system undergoes flutter or divergence type instability beyond a critical value of the force. The following non-dimensional parameters are introduced to facilitate the analysis.

$$\begin{cases} \rho_r = \frac{\rho_i}{\rho_o}, E_r = \frac{E_i}{E_o}, \xi_1 = \frac{h}{r_2}, \xi_2 = \frac{l \sin \alpha}{r_2} \\ \beta = P \frac{(1-\nu^2)}{E_o h}, \lambda = \Lambda r_2 \sqrt{\frac{(1-\nu^2) \rho_o}{E_o}} \end{cases}, \quad (13)$$

where,  $\lambda = \mathcal{G} \pm i\omega$  with  $\omega \geq 0$ .

The lowest magnitude of the follower force, for which an instability occurs is the critical load ( $P_{cr}$ ). The corresponding non-dimensional value is denoted by  $\beta_{cr}$ . A numerical scheme is adopted from Barsoum [86] and modified to adaptively increment the load parameter to improve computational efficiency for determining the onset of instability and the respective critical load. The solution methodology is described in Algorithm C.1.

### 3. Numerical illustration

A computer program is developed in commercial software MATLAB for the finite element analysis of free vibration and dynamic instability of truncated conical shell subjected to follower force. The vibration characteristics and critical load for instability are presented subsequently by adopting representative values of the pertinent non-dimensional parameters of Eq. (13) for the conical shell geometry, as adopted in aerospace applications. The boundary conditions are denoted by F, S, and C for the free, simply supported, and clamped cases, respectively, at each end of the shell. The subscripts S and L refers to the smaller and larger ends of the shell, respectively. The presentation is made using the following subsections.

#### 3.1. Convergence study

A convergence study is performed to determine the number of finite elements required to suitably represent the cases of homogeneous and FGM shells for different parameter values. For this, only the mass and elastic stiffness matrices are retained in Eq. (12) for the free vibration eigen analysis. The constituent material properties for the FGM are adopted from Tornabene et al. [16] and Zhao and Liew [87], as furnished in Table 1. The value of the Poisson's ratio is assumed to be constant as 0.3.

The undamped natural frequencies of the first few modes are determined considering varying finite element discretization of the shell geometry. The convergence results of the five lowest non-dimensional frequencies are given in Table 2 for a homogeneous shell for two boundary conditions (S<sub>S</sub>-S<sub>L</sub> and S<sub>S</sub>-C<sub>L</sub>) using the PFGM model with  $\eta \rightarrow \infty$  assuming any constituent material. Similarly, the convergence results for the five lowest cyclic frequencies are shown in Table 3 for two volume fraction indices of a PFGM truncated conical shell with aluminum as the outer constituent and ceramic – 2 as the inner constituent materials. The case with  $\eta \rightarrow \infty$  is numerically mimicked by adopting a large value of  $10^{30}$ .

The values in the brackets represent the corresponding circumferential and longitudinal mode numbers  $(n, m)$ .

**Table 1**

Properties of homogeneous constituents

Material	Poisson's ratio	Young's modulus	Density
Metal (Aluminum)	0.3	70 GPa	2707 kg/m <sup>3</sup>
Ceramic – 1 (Zirconia)	0.3	151 GPa	3000 kg/m <sup>3</sup>
Ceramic – 2	0.3	168 GPa	5700 kg/m <sup>3</sup>

The natural frequencies are observed to converge well for around 15 elements for both the homogeneous as well as FGM shells. Henceforth, both the free vibration and dynamic instability analyses employ 20 elements to reasonably discretize the shell geometry along its slanted length.

**Table 2**

Convergence of lowest non-dimensional undamped natural frequency ( $\omega$ ) of truncated conical shell with homogeneous material properties  $\alpha = 45^\circ$ ,  $\xi_1 = 0.01$ ,  $\xi_2 = 0.5$

Support	Number of elements				
	5	10	15	20	25
S <sub>S</sub> -S <sub>L</sub>	0.2275 (0,1)	0.2251 (0,1)	0.2240 (0,1)	0.2235 (0,1)	0.2233 (0,1)
S <sub>S</sub> -C <sub>L</sub>	0.3793 (6,1)	0.3744 (6,1)	0.3736 (6,1)	0.3734 (6,1)	0.3733 (6,1)

**Table 3**

Convergence of lowest undamped natural frequency ( $f$  in Hz) of truncated conical shell with PFGM model, F<sub>S</sub>-C<sub>L</sub> boundary,  $E_i = 168$  GPa,  $\rho_i = 5700$  kg/m<sup>3</sup>,  $E_o = 70$  GPa,  $\rho_o = 2707$  kg/m<sup>3</sup>,  $\alpha = 40^\circ$ ,  $\xi_1 = 0.0459$ ,  $\xi_2 = 0.7705$ ,  $r_2 = 2.178$  m

$\eta$	Number of elements				
	5	10	15	20	25
1	206.09 (2,1)	204.99 (2,1)	204.85 (2,1)	204.81 (2,1)	204.80 (2,1)
50	199.92 (2,1)	198.86 (2,1)	198.74 (2,1)	198.70 (2,1)	198.69 (2,1)

### 3.2. Verification of results

In this section, the results from the free vibration analyses are verified against the ones reported in literature for the homogeneous and the PFGM truncated conical shells. The non-dimensional undamped free vibration frequencies of the first longitudinal mode ( $m = 1$ ) for homogeneous truncated conical shell are compared with Irie et al. [9], Shu [13] and Liew et al. [14] (for different boundary conditions) in Table 4. For higher circumferential modes, the frequencies obtained from the present analysis are lower than that from the literature due to inclusion of the effect of rotary inertia in the present formulation.

The C<sub>S</sub>-F<sub>L</sub> boundary condition is used in this work to determine the free vibration and stability characteristics under follower force. To check the validity for this boundary condition, the non-dimensional natural frequencies with C<sub>S</sub>-F<sub>L</sub> boundary condition for different  $\alpha$  and  $\xi_2$  values are presented and compared with Irie et al. [9] in Table 5 for homogeneous material.

**Table 4**

Non-dimensional undamped natural frequency ( $\omega$ ) of truncated conical shell with homogeneous material,  $\alpha = 45^\circ$ ,  $\xi_1 = 0.01$ ,  $\xi_2 = 0.5$ ,  $m = 1$

$n$	Present	Irie et al. [9]	Shu [13]	Liew et al. [14]	Present	Irie et al. [9]	Shu [13]	Liew et al. [14]
	S <sub>S</sub> -S <sub>L</sub>				S <sub>S</sub> -C <sub>L</sub>			
0	0.2235	0.2233	0.2233	0.2234	0.8699	0.8698	0.8700	0.8691
1	0.5462	0.5462	0.5463	0.5462	0.8117	0.8117	0.8118	0.8113
2	0.6309	0.6310	0.6310	0.6309	0.6613	0.6614	0.6613	0.6610
3	0.5062	0.5065	0.5062	0.5061	0.5247	0.5249	0.5246	0.5244
4	0.3941	0.3947	0.3942	0.3941	0.4319	0.4324	0.4319	0.4316
5	0.3337	0.3348	0.3340	0.3337	0.3825	0.3834	0.3826	0.3822
6	0.3233	0.3248	0.3239	0.3235	0.3734	0.3747	0.3737	0.3732
7	0.3505	0.3524	0.3514	0.3510	0.3980	0.3997	0.3987	0.3980
8	0.4012	0.4033	0.4023	0.4019	0.4469	0.4489	0.4479	0.4472
9	0.4660	0.4684	0.4676	0.4671	0.5120	0.5142	0.5133	0.5124

**Table 5**

Non-dimensional undamped natural frequency ( $\omega$ ) of truncated conical shell with homogeneous material, C<sub>S</sub>-F<sub>L</sub> boundary,  $\xi_1 = 0.01$ ,  $m = 1$

$n$	Present	Irie et al. [9]	Present	Irie et al. [9]	Present	Irie et al. [9]
	$\xi_2 = 0.25, \alpha = 30^\circ$		$\xi_2 = 0.25, \alpha = 45^\circ$		$\xi_2 = 0.25, \alpha = 60^\circ$	
0	0.8311	0.8312	0.6857	0.6859	0.4965	0.4966
1	0.6767	0.6768	0.6220	0.6221	0.4671	0.4672
2	0.4831	0.4831	0.5038	0.5039	0.4057	0.4059
3	0.3551	0.3553	0.4040	0.4042	0.3477	0.3480
$n$	$\xi_2 = 0.75, \alpha = 30^\circ$		$\xi_2 = 0.75, \alpha = 45^\circ$		$\xi_2 = 0.75, \alpha = 60^\circ$	
0	0.2267	0.2266	0.3205	0.3205	0.3926	0.3926
1	0.1187	0.1182	0.1576	0.1574	0.1502	0.1500
2	0.0549	0.0549	0.0780	0.0779	0.0772	0.0771
3	0.0458	0.0469	0.0573	0.0579	0.0590	0.0593

The first five natural frequencies for PFGM truncated conical shell with aluminum as outer constituent and ceramic – 2 as inner constituent are determined for different values of  $\eta$  with F<sub>S</sub>-C<sub>L</sub> support condition. These are shown in Table 6 and compared with the results reported by Tornabene et al. [16]. It can be seen that the frequencies in a particular mode are highest when a shell is composed entirely of ceramic material ( $\eta = 0$ ) and becomes lowest

for a homogeneous shell made up of aluminum ( $\eta \rightarrow \infty$ ). This is because the effect of an increase in Young's modulus on the frequency in a ceramic shell is more pronounced than the effect of increased density when compared with the metallic shell, i.e.,  $E_r > \rho_r$ .

The results from Table 4, Table 5 and Table 6 show that the natural frequencies obtained from the present analysis for homogeneous or FGM truncated conical shells are in good agreement with the ones in existing literature.

**Table 6**

Undamped cyclic natural frequency ( $f$  in Hz) of truncated conical shell with PFGM model, FS-CL boundary,  $E_i = 168$  GPa,  $\rho_i = 5700$  kg/m<sup>3</sup>,  $E_o = 70$  GPa,  $\rho_o = 2707$  kg/m<sup>3</sup>,  $\alpha = 40^\circ$ ,  $\xi_1 = 0.0459$ ,  $\xi_2 = 0.7705$ ,  $r_2 = 2.178$  m

$f$ (Hz)	Present $\eta = 0$ (Ceramic)	Tornabene et al. [16]	Present $\eta = 0.6$	Tornabene et al. [16]
1	210.03 (2,1)	209.99	205.88 (2,1)	205.96
2	232.09 (3,1)	231.96	225.63 (3,1)	225.52
3	288.09 (4,1)	287.48	278.52 (4,1)	277.93
4	322.67 (1,1)	322.57	317.89 (1,1)	318.18
5	357.28 (2,2)	356.95	349.57 (2,2)	349.48
$f$ (Hz)	$\eta = 1$		$\eta = 5$	
1	204.81 (2,1)	204.91	203.84 (2,1)	203.93
2	224.56 (3,1)	224.44	227.86 (3,1)	227.67
3	277.29 (4,1)	276.66	285.02 (4,1)	284.26
4	315.93 (1,1)	316.32	309.19 (1,1)	309.57
5	347.72 (2,2)	347.66	347.21 (2,2)	347.08
$f$ (Hz)	$\eta = 20$		$\eta = 50$	
1	200.72 (2,1)	200.79	198.70 (2,1)	198.73
2	224.39 (3,1)	224.29	220.97 (3,1)	220.86
3	280.71 (4,1)	280.15	275.47 (4,1)	274.93
4	304.93 (1,1)	305.04	303.46 (1,1)	303.46
5	342.02 (2,2)	341.87	338.32 (2,2)	338.11
$f$ (Hz)	$\eta = 100$		$\eta \rightarrow \infty$ (Metal)	
1	197.80 (2,1)	197.79	196.73 (2,1)	196.69
2	219.34 (3,1)	219.21	217.39 (3,1)	217.23
3	272.92 (4,1)	272.38	269.85 (4,1)	269.28
4	302.87 (1,1)	302.83	302.24 (1,1)	302.14
5	336.64 (2,2)	336.39	334.65 (2,2)	334.35

### 3.3. Free vibration characteristics

The free vibration characteristics of the truncated conical shells are briefly reviewed in this section with special emphasis on the natural frequencies. This is because these modes have important bearing or participation in dynamic instabilities in the form of flutter. Henceforth, the PFGM and EFGM truncated conical shells are assumed to be composed of

aluminum and zirconia along the outer and inner surfaces respectively, along with  $C_S-F_L$  boundary condition. The relevant material properties are given in Table 1.

The choice of the constituent materials for the FGM is logical since, in the exit cones of launch vehicles, the inner lining of the conical surface is exposed to very high temperatures from the exhaust of the rocket engines. In such cases, ceramics like zirconia can be effectively used as a heat-resistant material. Additionally, aluminum can be employed as a lightweight material on the outer surface of the FGM. In order to simulate the boundaries of a rocket nozzle, the smaller end is taken as clamped, where it is typically welded or forged to the body of the launch vehicle. The larger end of the shell is kept free.

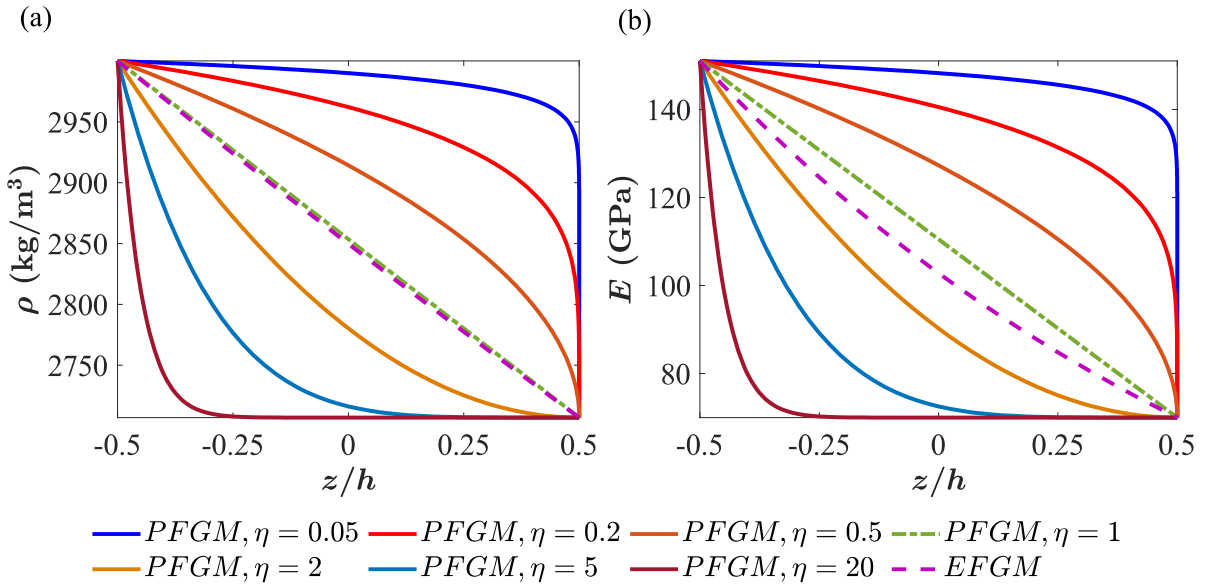


**Fig. 2.** Comparison of density ( $\rho$ ) and Young's modulus ( $E$ ) across non-dimensional thickness ( $z/h$ ) for EFGM and PFGM with varying volume fraction index ( $\eta$ ) having aluminum and zirconia as outer and inner constituents respectively: (a)  $\rho$  vs  $z/h$ ; (b)  $E$  vs  $z/h$ .

The thickness-wise variation of the density and Young's modulus for the PFGM and EFGM shells are shown in Fig. 2. The plots of PFGM are as per Eq. (1), while those of EFGM are obtained from Eq. (2) respectively. For the PFGM model, the density and Young's modulus at any depth are dependent on the volume fraction index  $\eta$ . For EFGM, the variation between the two surfaces is almost linear for density, whereas the Young's modulus shows a slight nonlinear variation for the chosen materials. The free vibration and stability behavior of the EFGM model is expected to be identical to that of the PFGM with  $\eta = 1$ .

Fig. 3 shows the non-dimensional natural frequencies of the first four longitudinal modes of the PFGM and EFGM shells for different semi-vertex angles ( $\alpha$ ) with two



damping ratios ( $\zeta = 0, 0.2$ ) considering the first circumferential mode ( $n = 0$ ). The non-dimensional natural frequencies of the first four circumferential modes with varying semi-vertex angles of the cone and the abovementioned damping ratios for the first longitudinal mode ( $m = 1$ ) are given in Fig. D.1. The curves for intermediate damping ratios lie between the two  $\zeta$  curves. The damped natural frequencies do not differ significantly from the undamped frequencies even at 20 percent damping, which is an unrealistically large value of damping for FGM in practical cases and is assumed here only for illustration. This variation is almost negligible in case of the first two longitudinal modes. Further, it is also found that for lower  $\alpha$ , the disparity between the damped and undamped frequencies is even smaller as compared to that at large  $\alpha$ .

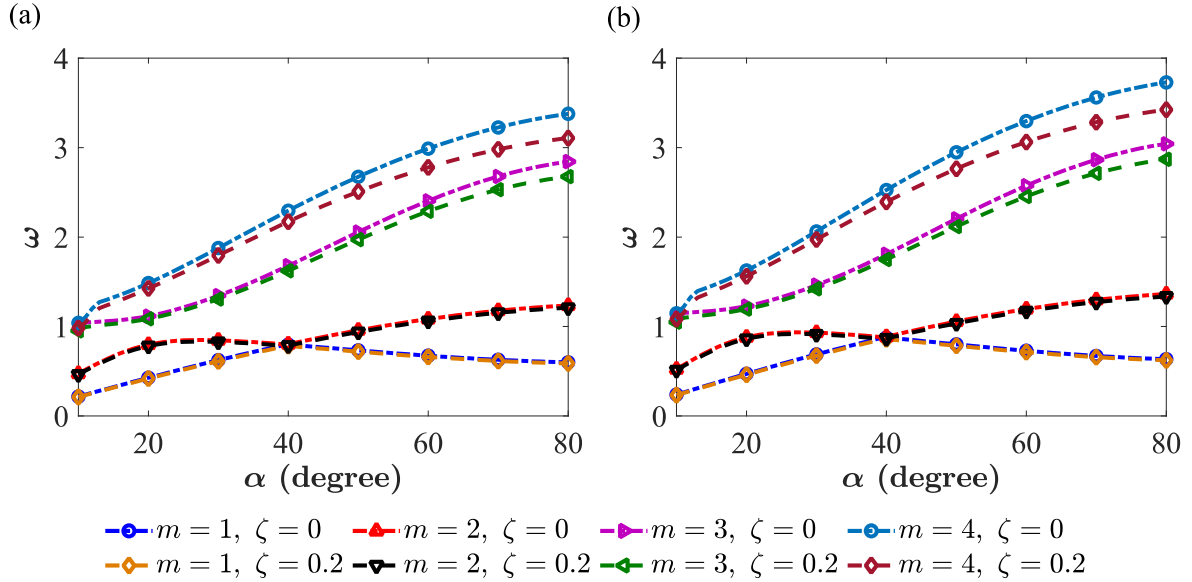


**Fig. 3.** The effect of damping on non-dimensional frequency ( $\omega$ ) with varying semi-vertex angle ( $\alpha$ ), longitudinal mode ( $m$ ), damping ratio ( $\zeta$ ) for circumferential mode ( $n = 0$ ), thickness parameter ( $\xi_1$ ) = 0.15, slenderness parameter ( $\xi_2$ ) = 0.5: (a) PFGM with volume fraction index ( $\eta$ ) = 5; (b) EFGM.

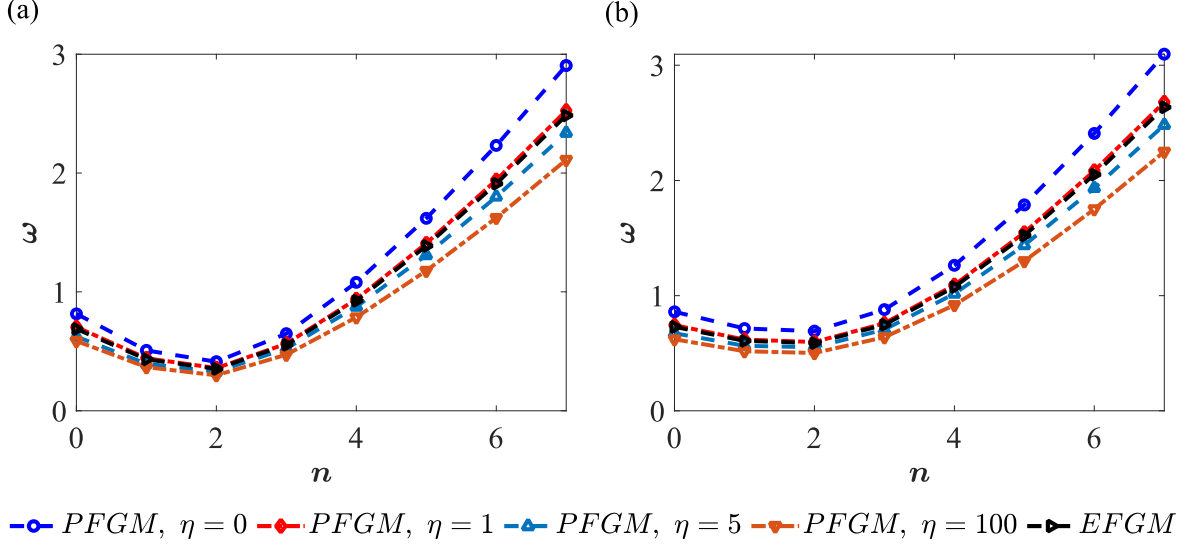


**Fig. 4.** The non-dimensional frequency ( $\omega$ ) variation with circumferential mode ( $n$ ) for EFGM and PFGM with varying volume fraction index ( $\eta$ ), thickness parameter ( $\xi_1$ ) = 0.15, slenderness parameter ( $\xi_2$ ) = 0.5, damping ratio ( $\zeta$ ) = 0, longitudinal mode ( $m$ ) = 1 and different semi-vertex angle ( $\alpha$ ): (a)  $\alpha = 30^\circ$ ; (b)  $\alpha = 60^\circ$ .

The variation of the first non-dimensional longitudinal frequency with different circumferential modes shows bath tub shapes in Fig. 4. The natural frequencies decrease for increasing values of  $\eta$  with the chosen constituents due to the reason discussed in the preceding section, i.e.,  $E_r > \rho_r$ . The lowest frequencies occur at circumferential modes  $n = 2, 2$  for  $\alpha = 30^\circ, 60^\circ$  respectively. It is also interesting to note that the circumferential mode corresponding to the lowest frequency does not change with change in the  $\eta$  values. The mode shapes corresponding to the circumferential modes  $n = 0$  (first) and  $n = 1$  (second) are referred as the ‘breathing’ and ‘flexural’ modes, respectively.

### 3.4. Dynamic instability analysis

For the dynamic instability analysis of truncated conical shell, non-zero magnitude of the constant follower force is adopted while solving the eigenvalue problem of Eq. (12). For determination of the critical load, up to four circumferential ( $n = 0, 1, 2, 3$ ) and four longitudinal modes ( $m = 1, 2, 3, 4$ ) are considered for the undamped and damped cases of the shell. Analysis of the higher modes may require higher-order shear deformation theories, for improved accuracy in the estimation of the displacement fields. In the absence of damping, the dynamic instabilities obtained in the present analysis are strictly flutter-type. For this

instability, two frequencies ( $\omega$ ) of the same circumferential mode ( $n$ ) coalesce for a certain magnitude of the follower force. Presence of this follower force results in the real part of  $\lambda$  being positive ( $\mathcal{G} > 0$ ). This causes the shell to experience motion with increasing amplitude under the constant follower force with progress in time.

For the damped structures, the system eigenvalues are twice in number as compared to the undamped case. In this case, flutter is not characterized by merging of two values of  $\omega$ . Instead, only the real part of  $\lambda$  becomes greater than zero. Divergence is characterized by zero system frequency ( $\omega = 0$ ), and  $\mathcal{G} > 0$  in both damped and undamped shells. Algorithm C.1 ensures the eigenvalues are initially sorted by the magnitude of  $\lambda$  for determining the longitudinal modes for any follower force. Both flutter and divergence type instability have been found to occur for damped system. The flutter instability is seen to be critical for all observed parameter values as it occurs under a lower magnitude of the follower force.

Fig. 5(a) shows the plots of the real and imaginary parts of the non-dimensional eigenvalue for undamped truncated conical shell subjected to different non-dimensional load with characteristic geometry and material parameters. It shows the coalescence of the third and fourth longitudinal mode frequencies ( $m = 3, 4$ ) accompanied by positive real part.

Weak flutter instabilities are observed for certain combination of the parameter values. The magnitude of follower force value for a weak flutter is considerably lower than the general trend of the flutter load in the parameter space. These weak instabilities disappear on increasing the follower force magnitude beyond a particular value, unlike strong flutter instability. Subsequent to this, a strong flutter is again observed at a higher magnitude of the follower force, which does not go away on increasing the magnitude of the force. Instances of weak flutter and subsequent strong flutter are shown in Fig. 5(b) considering an undamped shell. The second and third longitudinal modes coalesce initially for a certain value of the follower force, indicating weak flutter. However, the coalesced eigenpath bifurcates subsequently into two distinct eigenpaths at a higher magnitude of the follower force. On further increasing the follower force, the first and second frequencies are seen to coalesce to give rise to a strong flutter instability.

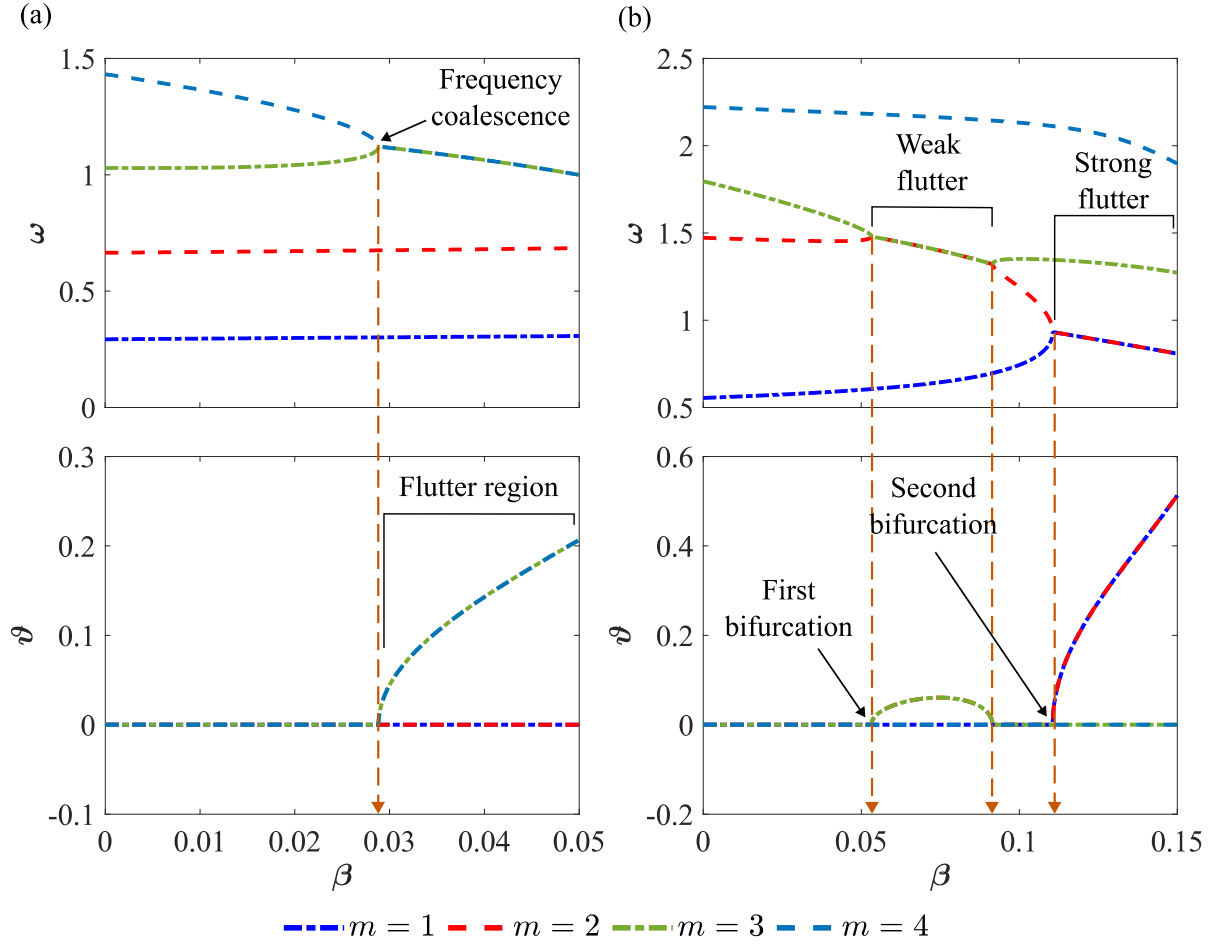


**Fig. 5.** Flutter instability showing real ( $\vartheta$ ) and imaginary ( $\omega$ ) parts of non-dimensional eigenvalue for changing non-dimensional load ( $\beta$ ) and longitudinal mode ( $m$ ) of undamped ( $\zeta=0$ ) PFGM shell with different circumferential mode ( $n$ ), volume fraction index ( $\eta$ ), semi-vertex angle ( $\alpha$ ), thickness parameter ( $\xi_1$ ), slenderness parameter ( $\xi_2$ ): (a)  $n=0$ ,  $\eta=10$ ,  $\alpha=30^\circ$ ,  $\xi_1=0.1$ ,  $\xi_2=0.7$ ; (b)  $n=1$ ,  $\eta=5$ ,  $\alpha=30^\circ$ ,  $\xi_1=0.16$ ,  $\xi_2=0.4$ .

The weak flutter instabilities are significantly suppressed in the presence of damping. At higher damping values, such weak instabilities get suppressed even more, and the plot of the critical load becomes a smooth curve in the parametric space. It can be attributed to the fact that the stability of the structure enhances with increased damping as it helps in the dissipation of energy in the system through alternate path resulting in higher critical loads.

The non-dimensional load corresponding to the identical circumferential wave numbers and identical coalescing longitudinal modes follows smooth curves, as presented in Fig. 6. The isolated points indicate that they are not part of any of the plotted eigenmodes. The envelope is the critical load curve in the parametric space obtained by joining the lowest non-dimensional loads corresponding to each parameter value.

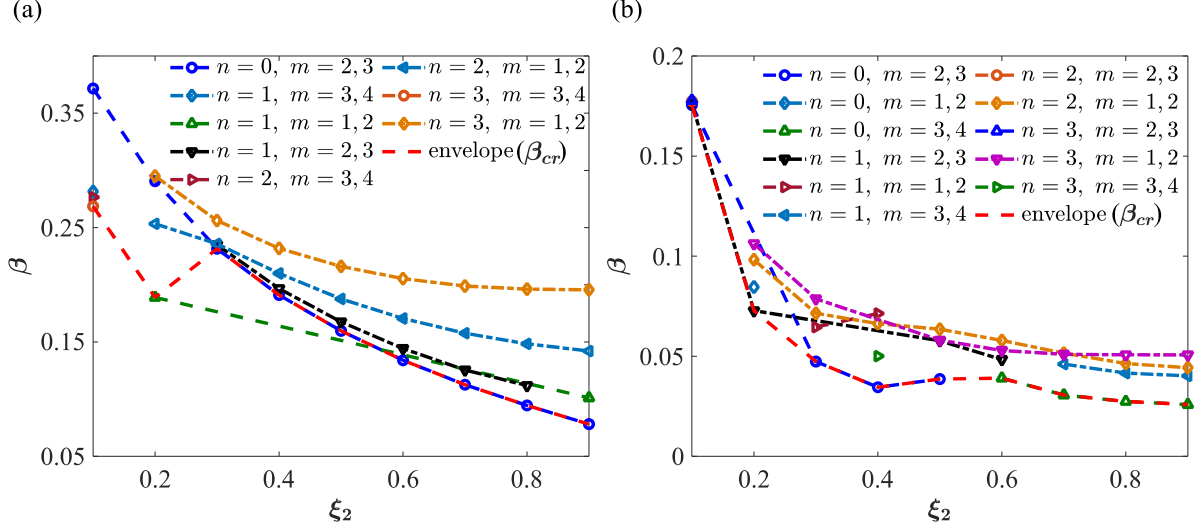


**Fig. 6.** Curves of identical eigenmodes and envelope of non-dimensional load ( $\beta$ ) of PFGM with varying slenderness parameter ( $\xi_2$ ), semi-vertex angle ( $\alpha$ ), thickness parameter ( $\xi_1$ ) for volume fraction index ( $\eta$ )=5, damping ratio ( $\zeta$ )=0: (a)  $\alpha = 80^\circ$ ,  $\xi_1 = 0.25$ ; (b)  $\alpha = 30^\circ$ ,  $\xi_1 = 0.1$ .

### 3.5. Influence of parametric variations on the flutter load

This section presents the parametric study of the non-dimensional flutter load considering different geometry, damping, and functional gradations of the FG truncated conical shell. The variation of the critical non-dimensional flutter load  $\beta_{cr}$  for different gradation index  $\eta$  are shown in Fig. 7 for changing  $\xi_2$ ,  $\xi_1$ ,  $\alpha$ ,  $\zeta$  values. Common to all these plots is the reducing critical load with increasing metallic content, marked by higher gradient index. The trend can be attributed to the fact that the non-dimensional frequencies of the truncated conical shell decrease for higher volume fraction indices as illustrated in Fig. 4. Although, the maximum critical load is observed for ceramic, yet functional gradation is desirable to incorporate the lightweight metallic constituent in the shell. The results are presented hereafter for only two values of  $\eta$ , namely  $\eta = 1$  and  $\eta = 5$ . The former ( $\eta = 1$ ) gives a linear variation of the volume fraction in the FGM.

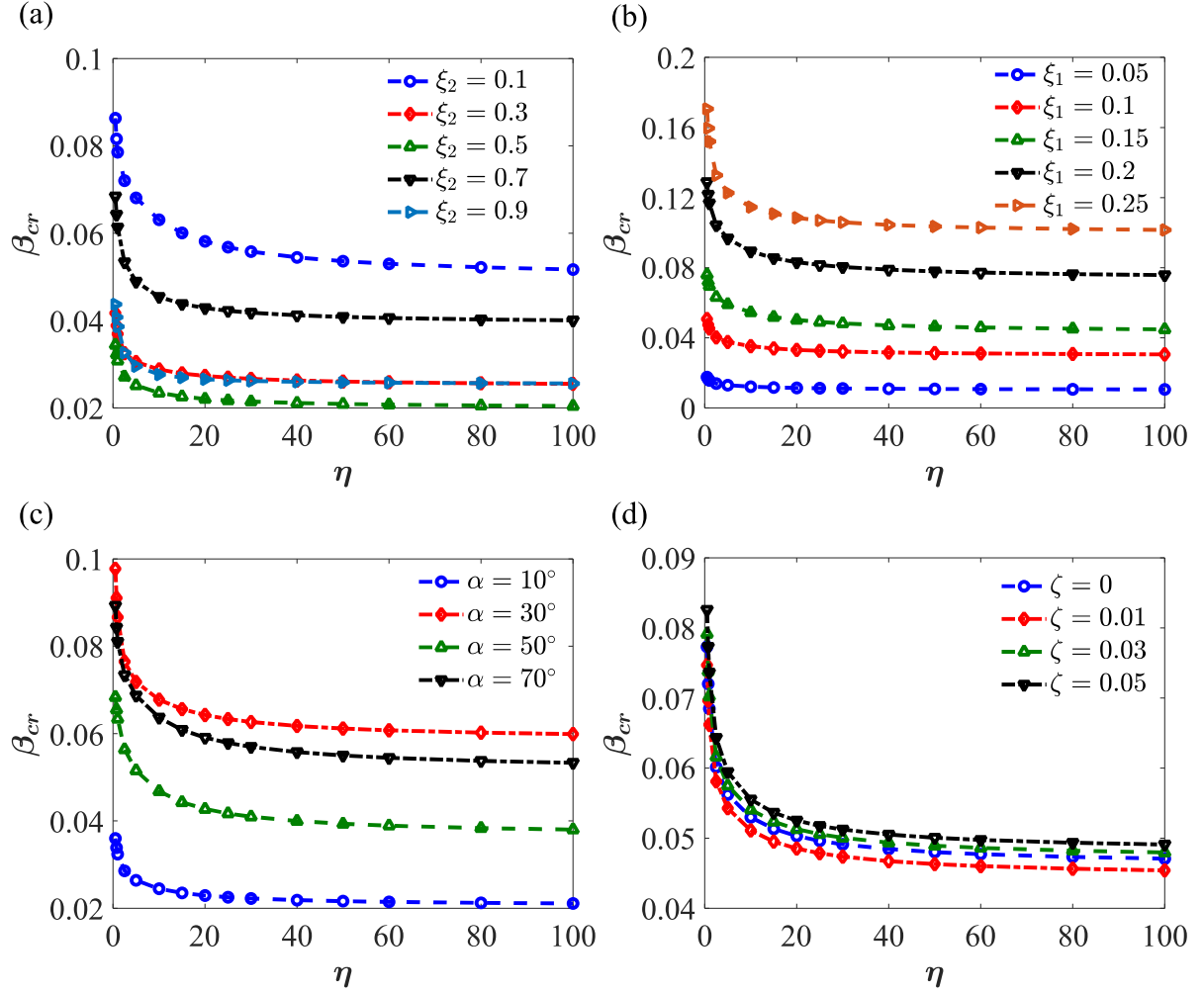


**Fig. 7.** The dependence of non-dimensional critical load ( $\beta_{cr}$ ) on volume fraction index ( $\eta$ ) of PFGM for different slenderness parameter ( $\xi_2$ ), thickness parameter ( $\xi_1$ ), semi-vertex angle ( $\alpha$ ), damping ratio ( $\zeta$ ): (a)  $\zeta = 0$ ,  $\alpha = 10^\circ$ ,  $\xi_1 = 0.15$ ; (b)  $\zeta = 0$ ,  $\alpha = 60^\circ$ ,  $\xi_2 = 0.6$ ; (c)  $\zeta = 0$ ,  $\xi_1 = 0.15$ ,  $\xi_2 = 0.6$ ; (d)  $\alpha = 40^\circ$ ,  $\xi_1 = 0.15$ ,  $\xi_2 = 0.9$ .

Fig. 8 presents the non-dimensional critical load for varying values of the thickness parameter ( $\xi_1$ ) with different level of damping ( $\zeta = 0, 0.01, 0.03, 0.05$ ). The critical load increases with higher damping ratios. However, the increase in the critical load beyond around three percent damping is negligible. As discussed in the previous section, the sudden drops in the load parameter for low  $\zeta$  values are due to the formation of weak flutter instabilities, which gets stabilized with increased damping. The curves for  $\zeta = 0$  should ideally always be below the other  $\zeta$  curves, but this is not observed for Fig. 8(b). Such anomalous behavior can be attributed to the fact that the present analysis includes only the first four longitudinal modes. Many more weak instabilities could be found, if higher longitudinal modes are included in the analysis. This would have caused the  $\zeta = 0$  curve to

lie below the higher  $\zeta$  curves. From Fig. 7, it can be seen that there are no drops in the critical load due to weak flutter for different gradation indices with any parameter value. Consequently, it can be said that the weak flutter instabilities are not much influenced by the PFGM gradation index and they tend to lie in identical regions of the parametric space for different values of  $\eta$  (see Fig. D.2). Subsequent results are presented herein by taking three percent damping in the first two modes, which is reasonable for all practical purposes.

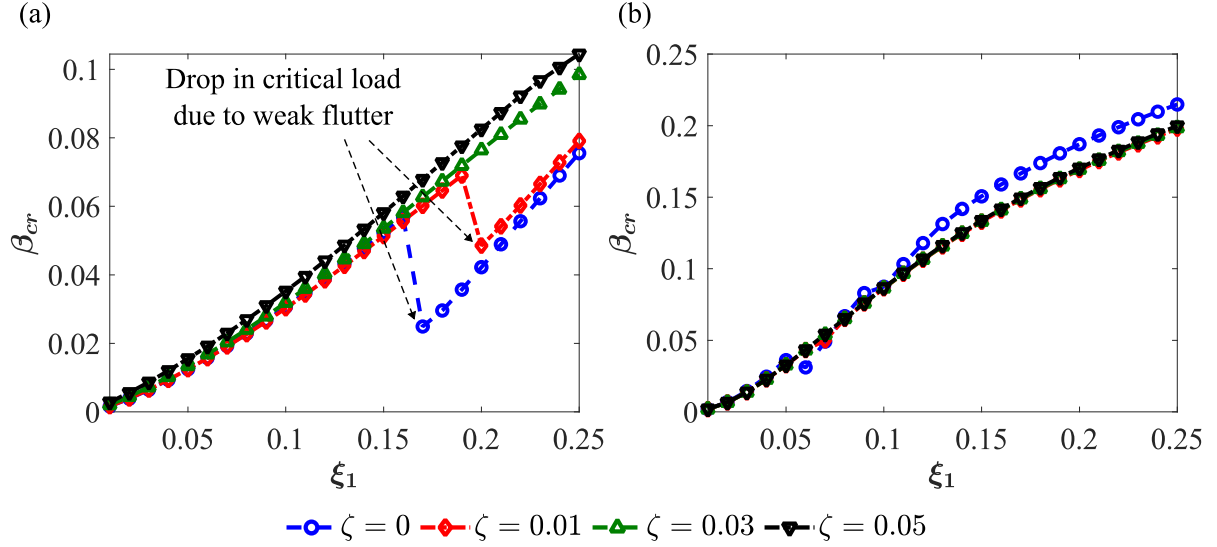


**Fig. 8.** The effect of damping on non-dimensional critical load ( $\beta_{cr}$ ) of PFGM of volume fraction index ( $\eta$ )=5 with different thickness parameter ( $\xi_1$ ), damping ratio ( $\zeta$ ), slenderness parameter ( $\xi_2$ ), semi-vertex angle ( $\alpha$ ): (a)  $\xi_2 = 0.7$ ,  $\alpha = 30^\circ$ ; (b)  $\xi_2 = 0.3$ ,  $\alpha = 60^\circ$ .

The change in non-dimensional critical load ( $\beta_{cr}$ ) for PFGM with different thickness parameter ( $\xi_1$ ), slenderness parameter ( $\xi_2$ ), and semi-vertex angle ( $\alpha$ ) are shown in Fig. 9. An increase in critical load with increasing thickness parameter is seen, which is evident as thicker shells exhibit instability under larger magnitude of follower force, if other parameters remain constant. The critical loads are lower for shells with higher values of slenderness parameter for any range of the semi-vertex angle. Increased  $\xi_2$  keeping other parameters constant implies the shell is longer and hence becomes more susceptible to instability. Moreover, weak instabilities are not frequent for shells having large  $\xi_2$  values. This is because such shells being longer are comparatively more unstable. Hence the onset of any flutter instability is expected to grow and dominate as a strong flutter in the system.

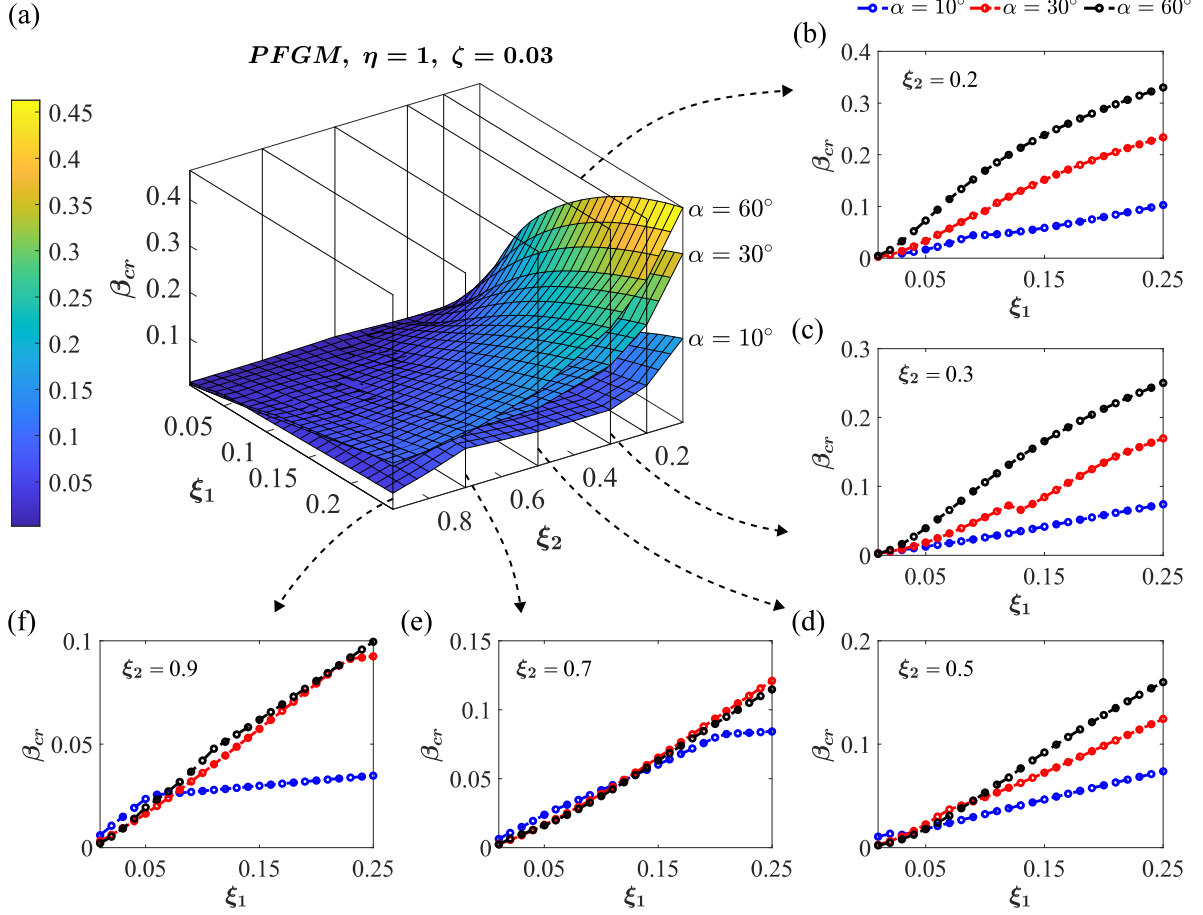


**Fig. 9.** Non-dimensional critical load ( $\beta_{cr}$ ) of PFGM for different thickness parameter ( $\xi_1$ ), slenderness parameter ( $\xi_2$ ), semi-vertex angle ( $\alpha$ ) with volume fraction index ( $\eta$ )=1, damping ratio ( $\zeta$ )=0.03: (a) surface plot showing parametric variation of  $\beta_{cr}$ ; figures (b) to (f) showing sections from  $\beta_{cr} - \xi_1$  plane for different  $\xi_2$  values (b)  $\xi_2 = 0.2$ ; (c)  $\xi_2 = 0.3$ ; (d)  $\xi_2 = 0.5$ ; (e)  $\xi_2 = 0.7$ ; (f)  $\xi_2 = 0.9$ .

Roughly in the range of  $0.7 \leq \xi_2 \leq 0.9$  and  $\alpha \leq 40^\circ$  (Fig. 9(e) and (f)), the critical load parameter ( $\beta_{cr}$ ) attains saturation or varies negligibly beyond a certain  $\xi_1$ . Although  $\beta_{cr}$  remains constant, it does not imply that the dimensional critical load will also be constant. This is because the dimensional load is proportional to the thickness of the shell, and it increases linearly due to increasing  $\xi_1$ . Interestingly, a similar observation has also been reported in the case of a completely free cylindrical shell subjected to follower force by Park and Kim [72]. It follows from the present study that such a phenomenon of the constant non-dimensional critical load must also exist in the case of sufficiently long cylindrical shells under follower force with C<sub>S</sub>-F<sub>L</sub> boundary condition [74]. It is because a truncated conical shell with small  $\alpha$  and large  $\xi_2$  values can be approximated as a long cylindrical shell in the



limiting sense. Moreover, the parametric space shows a parabolic variation of  $\beta_{cr}$  with  $\xi_1$  in Fig. 9(b) and (c) for increasing semi-vertex angles ( $\alpha \geq 30^\circ$ ) and decreasing slenderness parameter ( $\xi_2$ ) of the FG shell. All parameters being identical, it can be said from Fig. 9 and Fig. D.3 that the critical loads in the EFGM model are close to the PFGM model with  $\eta = 1$ .

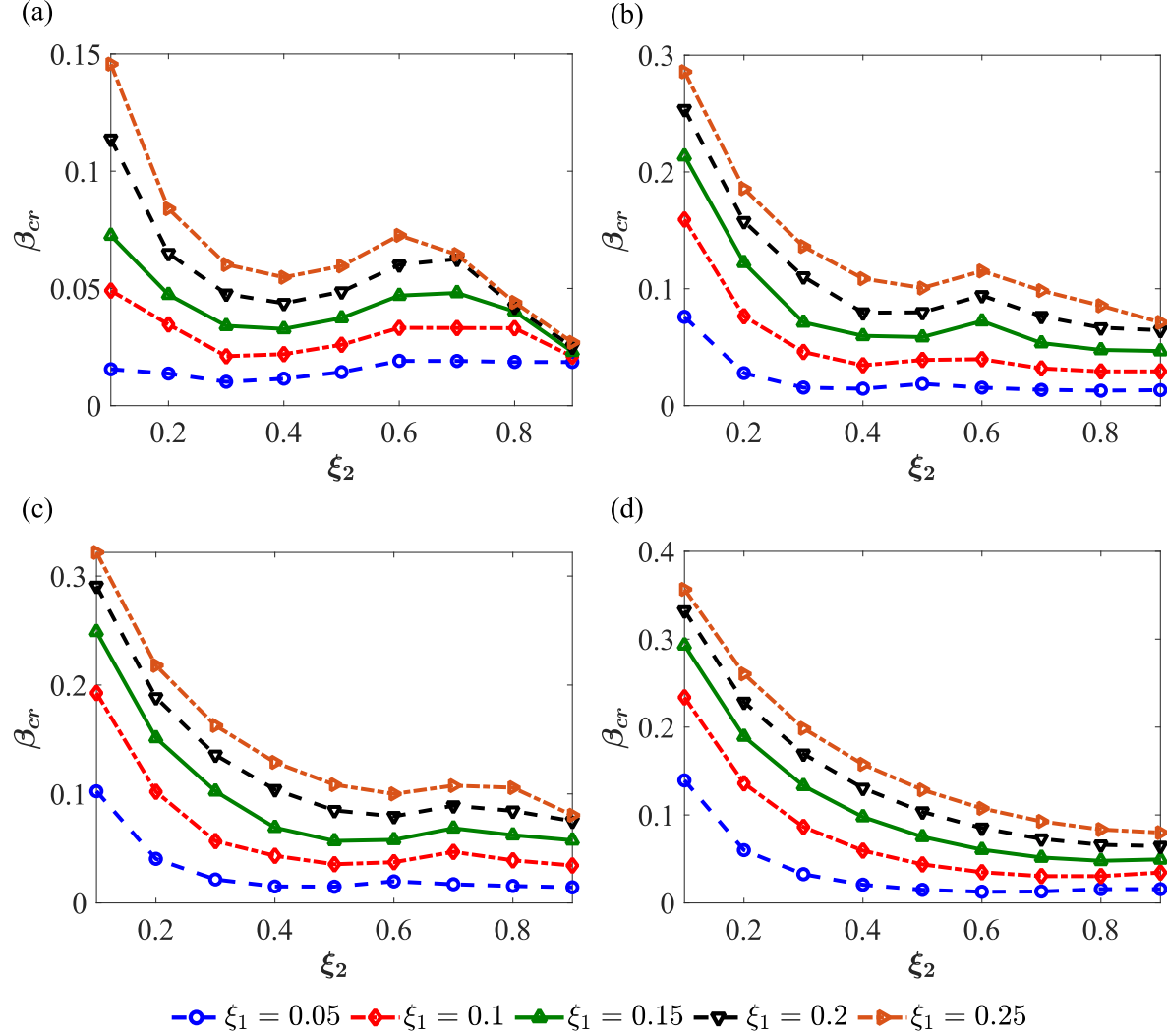


**Fig. 10.** Non-dimensional critical load ( $\beta_{cr}$ ) for varying slenderness parameter ( $\xi_2$ ) of PFGM with different thickness parameter ( $\xi_1$ ), different semi-vertex angle and volume fraction index ( $\eta$ )=5, damping ratio ( $\zeta$ )=0.03 and ( $\alpha$ ): (a)  $\alpha = 10^\circ$ ; (b)  $\alpha = 30^\circ$ ; (c)  $\alpha = 40^\circ$ ; (d)  $\alpha = 60^\circ$ .

Fig. 10 presents the variation of non-dimensional critical load ( $\beta_{cr}$ ) of PFGM with slenderness parameter ( $\xi_2$ ) for different semi-vertex angles ( $\alpha$ ). For a semi-vertex angle less than  $40^\circ$  and thickness parameter ( $\xi_1$ ) greater than 0.1, the critical flutter load ( $\beta_{cr}$ )

first decreases up to a particular slenderness parameter value ( $0.4 \leq \xi_2 \leq 0.6$ ) and then increases shortly before decreasing again. This reduction in the critical load after the rising part is because of a mode jump from a lower circumferential wave number to a higher mode, triggering the flutter. This is identical to the formation of an Arnold's tongue. These curves also merge for large  $\xi_2$  values because the non-dimensional critical load attains constant value for changing  $\xi_1$  as seen before. Keeping other parameters constant, the critical load is also found to increase with increasing semi-vertex angle of the conical shell. For other parametric values, the critical load decreases monotonically with increasing  $\xi_2$ . In general, the non-dimensional critical load of the truncated conical shell reduces for a decrease in the semi-vertex angle, reduction in thickness, or an increase in the length of the shell.

#### 4. Summary and conclusions

The stability behavior of FG truncated conical shells under follower force is presented by adopting a simple yet efficient finite element formulation. The analyses explain the effects of the shell geometry and material properties on the critical flutter load, expressed in terms of several non-dimensional parameters involving the geometry and material properties. The FG truncated conical shell is assumed to be clamped at the smaller edge and free at the larger edge and is subjected to a uniformly distributed follower force at the free end. Power-law and exponential functional gradations across the shell thickness are considered. A three-node Lagrange element discretization is adopted along the meridian, whereas harmonic basis is employed along the circumference for approximating the displacement field. A mesh convergence study is conducted to ascertain the suitable mesh size for discretization. The analysis is verified against the free vibration characteristics reported in earlier studies.

Mass and stiffness proportional damping is considered. The analysis under follower force reveals flutter-type instability in undamped shells, whereas both flutter and divergence instabilities occur for damped shells. The flutter happens for a lower magnitude of the follower force as compared to divergence. Many erratic weak instabilities are also observed for undamped and lightly damped shells, manifested as drastic drops in the load from the general trend of the critical flutter load in the parameter space. The weak flutter instabilities are not much influenced by the power-law gradation index. Long shells with small semi-vertex angles are relatively less susceptible to weak instabilities even though they exhibit a much lower critical load. It becomes imperative to perform instability analysis for undamped and lightly damped short truncated conical shells subjected to follower forces. The stability of

the shell is sensitive to even a slight perturbation in its geometric properties. Structural damping enhances stability by increasing the magnitude of the critical load, but its effect beyond three percent damping is almost negligible.

For a given circumferential wave numbers, the locus of a pair of identical coalescing (longitudinal) modes results in smooth envelope curves. The minima of all such flutter loads gives the general variation of the critical load in the parameter space. The critical flutter load for the PFGM shell decreases monotonically with increasing volume fraction index. The largest and smallest critical loads are observed for homogeneous shells with aluminum and zirconia. The non-dimensional critical load remains constant beyond a particular thickness parameter ( $\xi_1$ ) for long shells with low semi-vertex angles. The critical load decreases for increasing slenderness parameters ( $\xi_2$ ) except for small semi-vertex angles and thickness parameters ( $\xi_1$ ) greater than 0.1. In the latter case, the critical load drops initially, followed by an increasing trend before reducing again.

## Declaration of Competing Interest

The authors declare that they have no known competing financial interests or personal relationships that could have appeared to influence the work reported in this paper.

## Appendix A

$$\mathbf{D} = \begin{bmatrix} \frac{E}{1-\nu^2} & \frac{\nu E}{1-\nu^2} & 0 & 0 & 0 \\ \frac{\nu E}{1-\nu^2} & \frac{E}{1-\nu^2} & 0 & 0 & 0 \\ 0 & 0 & \frac{E}{2(1+\nu)} & 0 & 0 \\ 0 & 0 & 0 & \frac{E}{2(1+\nu)} & 0 \\ 0 & 0 & 0 & 0 & \frac{E}{2(1+\nu)} \end{bmatrix}. \quad (\text{A.1})$$

$$\mathbf{E} = \begin{bmatrix} \frac{\partial}{\partial s} & 0 & 0 & z \frac{\partial}{\partial s} & 0 \\ \frac{1}{s} & \frac{1}{s \sin \alpha} \frac{\partial}{\partial \theta} & \frac{1}{s \tan \alpha} & \frac{z}{s} & \frac{z}{s \sin \alpha} \frac{\partial}{\partial \theta} \\ \frac{1}{s \sin \alpha} \frac{\partial}{\partial \theta} & \frac{\partial}{\partial s} - \frac{1}{s} & 0 & \frac{z}{s \sin \alpha} \frac{\partial}{\partial \theta} & z \left( \frac{\partial}{\partial s} - \frac{1}{s} \right) \\ 0 & 0 & \frac{\partial}{\partial s} & 1 & 0 \\ 0 & -\frac{1}{s \tan \alpha} & \frac{1}{s \sin \alpha} \frac{\partial}{\partial \theta} & 0 & 1 \end{bmatrix} \quad (\text{A.2})$$

$$\begin{bmatrix} \gamma_1 \\ \gamma_2 \end{bmatrix} = \begin{bmatrix} \frac{1}{2\Omega_1} & \frac{\Omega_1}{2} \\ \frac{1}{2\Omega_2} & \frac{\Omega_2}{2} \end{bmatrix}^{-1} \begin{bmatrix} \zeta \\ \zeta \end{bmatrix}. \quad (\text{A.3})$$

$$\begin{cases} \mathbf{A} = -\mathbf{M}^{-1} (P(\mathbf{Q}_N - \mathbf{Q}_C) + \mathbf{K}), \mathbf{q} = \mathbf{d}, \mu = \Lambda^2 \text{ for } \zeta = 0 \\ \mathbf{A} = \begin{bmatrix} \mathbf{0} & \mathbf{I} \\ -\mathbf{M}^{-1} (P(\mathbf{Q}_N - \mathbf{Q}_C) + \mathbf{K}) & -\mathbf{M}^{-1} \mathbf{C} \end{bmatrix}, \mathbf{q} = \begin{bmatrix} \mathbf{d} \\ \Lambda \mathbf{d} \end{bmatrix}, \mu = \Lambda \text{ for } \zeta > 0 \end{cases}. \quad (\text{A.4})$$

## Appendix B

**Table B.1**

Classification of the eigenvalue solution

Type of motion	Nature of eigen solution
Harmonic motion with constant amplitude	$\Theta = 0, \Omega > 0$
Harmonic motion with decreasing amplitude (Damped vibration)	$\Theta < 0, \Omega > 0$
Harmonic motion with increasing amplitude (Flutter instability)	$\Theta > 0, \Omega > 0$
Divergence instability	$\Theta > 0, \Omega = 0$

## Appendix C

**Algorithm C.1**

Numerical scheme for load jump algorithm to determine critical follower load

1. Define shell parameters  $r_2, \alpha, \xi_1, \xi_2$ , number of elements, boundary condition
2. Define material properties  $\nu, E_i, E_r, \rho_i, \rho_r, \eta$  (for PFGM),  $\zeta$
3. Define required circumferential ( $n \equiv 0 \dots n_{max}$ ) and longitudinal ( $m \equiv 1 \dots m_{max}$ ) modes
4. Define minimum load increment parameter  $\beta_{inc}^{min} = 10^{-4}$ , maximum load increment parameter  $\beta_{inc}^{max}(\zeta = 0) = 10^{-3}$ ,  $\beta_{inc}^{max}(\zeta > 0) = 10^{-2}$ , load accuracy parameter  $\beta_{tol} = 10^{-6}$ , load jump factor  $j_\beta = 3$
5. For each  $n$ 
  - a. Evaluate  $\mathbf{M}, \mathbf{K}, \mathbf{Q}_C$  and  $\mathbf{Q}_N$  matrices
  - b. If  $\zeta > 0$ 
    - Compute first two natural frequencies keeping  $\mathbf{Q}_N - \mathbf{Q}_C = \mathbf{0}$

- Evaluate  $\gamma_1$ ,  $\gamma_2$  and  $\mathbf{C}$
- c. Initialize current load increment  $\beta_{inc}^{cur} = \beta_{inc}^{min}$ , load parameter  $\beta = \beta_{inc}^{cur}$
- d. To identify critical load, while (true) do
  - i. Evaluate  $P$
  - ii. If  $\zeta = 0$ 
    - Obtain  $\Lambda = \{\lambda \mid \lambda^2 \text{ is eigenvalue}\}$
    - Else if  $\zeta > 0$ 
      - Obtain  $\Lambda = \{\lambda \mid \lambda \text{ is eigenvalue}\}$
      - Redefine  $\Lambda \equiv \Lambda - \{\lambda \mid \text{Im}(\lambda) < 0 \forall \lambda \in \Lambda\}$
  - iii. Extract first  $m$  modes after sorting  $\Lambda$  by absolute magnitude
  - iv. Find the number of instability modes  $NIM = |\{\lambda \mid \text{Re}(\lambda) > 0 \forall \lambda \in \Lambda\}|$
  - v. If  $NIM = 0$ 
    - Set  $\beta_{prev} = \beta$
    - Set new increment  $\beta_{inc}^{cur} = j_\beta \beta_{inc}^{cur}$
    - If  $((\zeta = 0 \text{ and } \beta_{inc}^{cur} > \beta_{inc}^{max}(\zeta = 0)) \text{ or } (\zeta > 0 \text{ and } \beta_{inc}^{cur} > \beta_{inc}^{max}(\zeta > 0)))$ , set  $\beta_{inc}^{cur} = \beta_{inc}^{min}$
    - Set  $\beta = \beta_{prev} + \beta_{inc}^{cur}$
    - Else if  $(\zeta = 0 \text{ and } NIM > 2) \text{ or } (\zeta > 0 \text{ and } NIM > 1)$ 
      - Set  $\beta_{inc}^{cur} = \beta_{inc}^{cur} / j_\beta$
      - Set  $\beta = \beta_{prev} + \beta_{inc}^{cur}$
      - Else if  $(\zeta = 0 \text{ and } (NIM = 1 \text{ or } NIM = 2)) \text{ or } (\zeta > 0 \text{ and } NIM = 1)$ 
        - Set  $\beta_{range} = [\beta_{prev}, \beta]$
        - Exit while
  - e. To improve accuracy, while  $((\beta_{range}[2] - \beta_{range}[1]) > \beta_{tol})$  do
    - i. Compute  $\beta = (\beta_{range}[2] + \beta_{range}[1]) / 2$
    - ii. Evaluate  $P$
    - iii. If  $\zeta = 0$ 
      - Obtain  $\Lambda = \{\lambda \mid \lambda^2 \text{ is eigenvalue}\}$
      - Else if  $\zeta > 0$ 
        - Obtain  $\Lambda = \{\lambda \mid \lambda \text{ is eigenvalue}\}$
        - Redefine  $\Lambda \equiv \Lambda - \{\lambda \mid \text{Im}(\lambda) < 0 \forall \lambda \in \Lambda\}$
    - iv. Extract first  $m$  modes after sorting  $\Lambda$  by absolute magnitude
    - v. Find the number of instability modes  $NIM = |\{\lambda \mid \text{Re}(\lambda) > 0 \forall \lambda \in \Lambda\}|$
    - vi. If  $NIM > 0$ , set  $\beta_{range}[2] = \beta$   
Else set  $\beta_{range}[1] = \beta$
  - f. Set critical load for  $n^{th}$  mode  $\beta_{cr}^{(n)} = (\beta_{range}[2] + \beta_{range}[1]) / 2$
  - g. To check the type of instability

- If  $(\text{Re}(\lambda) > 0 \text{ and } \text{Im}(\lambda) \neq 0)$ , the instability mode is flutter-type
- Else if  $(\text{Re}(\lambda) > 0 \text{ and } \text{Im}(\lambda) = 0)$ , the instability mode is divergence-type

6. The least of all  $\beta_{cr}^{(n)}$  for different  $n$  gives  $\beta_{cr}$

Note:  $|\cdot|$  denotes cardinality of the set

## Appendix D

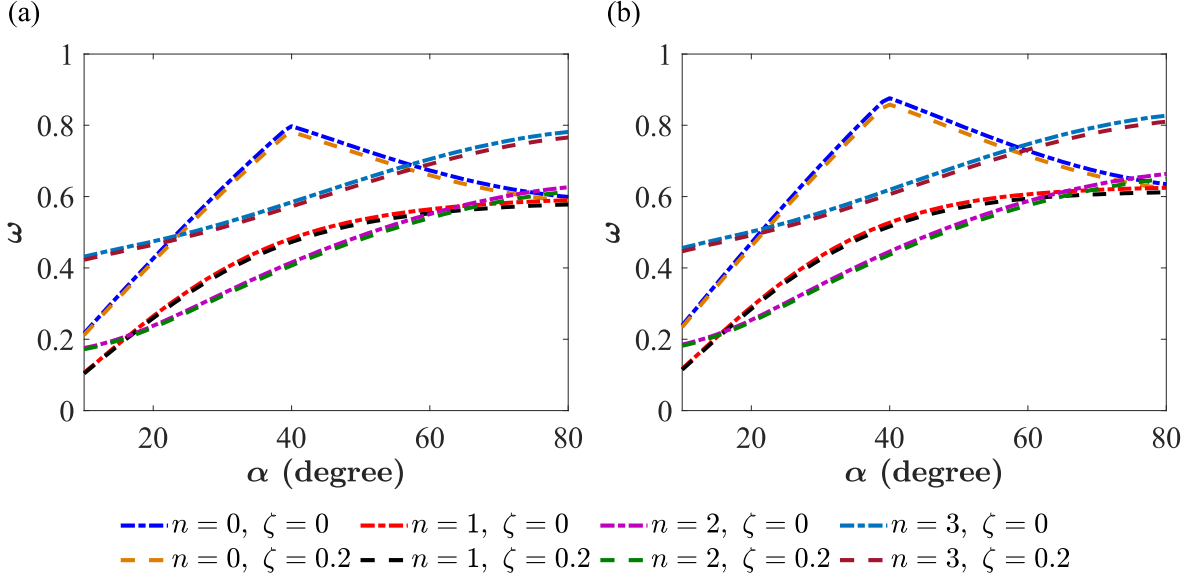


**Fig. D.1.** The effect of damping on non-dimensional frequency ( $\omega$ ) with varying semi-vertex angle ( $\alpha$ ), circumferential mode ( $n$ ), damping ratio ( $\zeta$ ) for longitudinal mode ( $m$ )=1, thickness parameter ( $\xi_1$ )=0.15, slenderness parameter ( $\xi_2$ )=0.5: (a) PFGM with volume fraction index ( $\eta$ )=5; (b) EFGM.

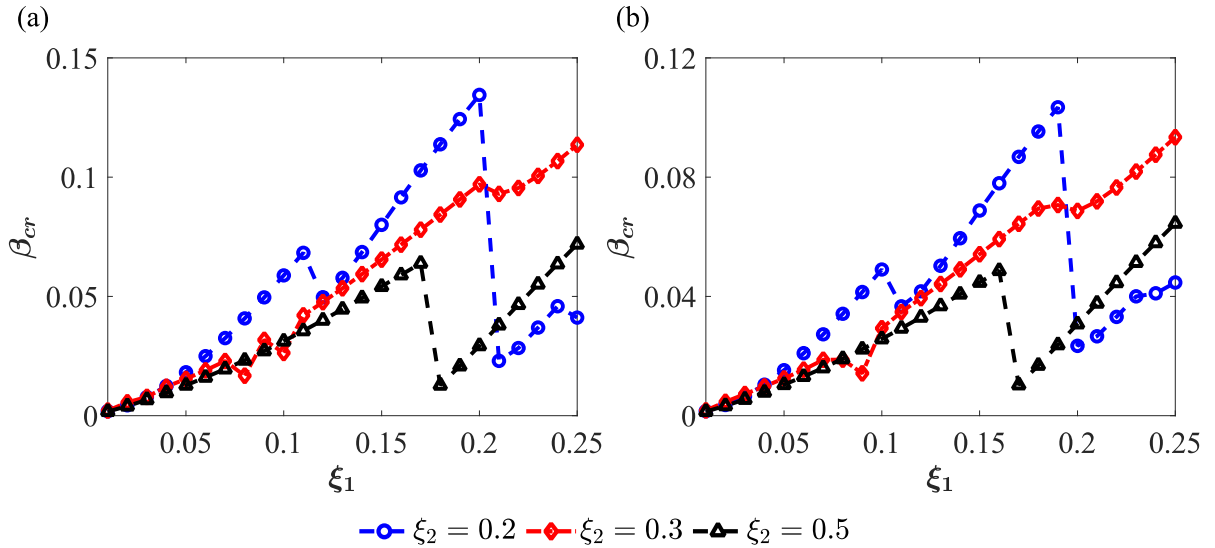


**Fig. D.2.** Identical regions of drop in non-dimensional critical load ( $\beta_{cr}$ ) due to weak flutter instabilities in PFGM for two volume fraction indices ( $\eta$ ) with damping ratio ( $\zeta$ )=0, semi-

vertex angle ( $\alpha$ ) =  $20^\circ$  and different thickness parameter ( $\xi_1$ ), slenderness parameter ( $\xi_2$ ):  
(a)  $\eta = 1$ ; (b)  $\eta = 5$ .

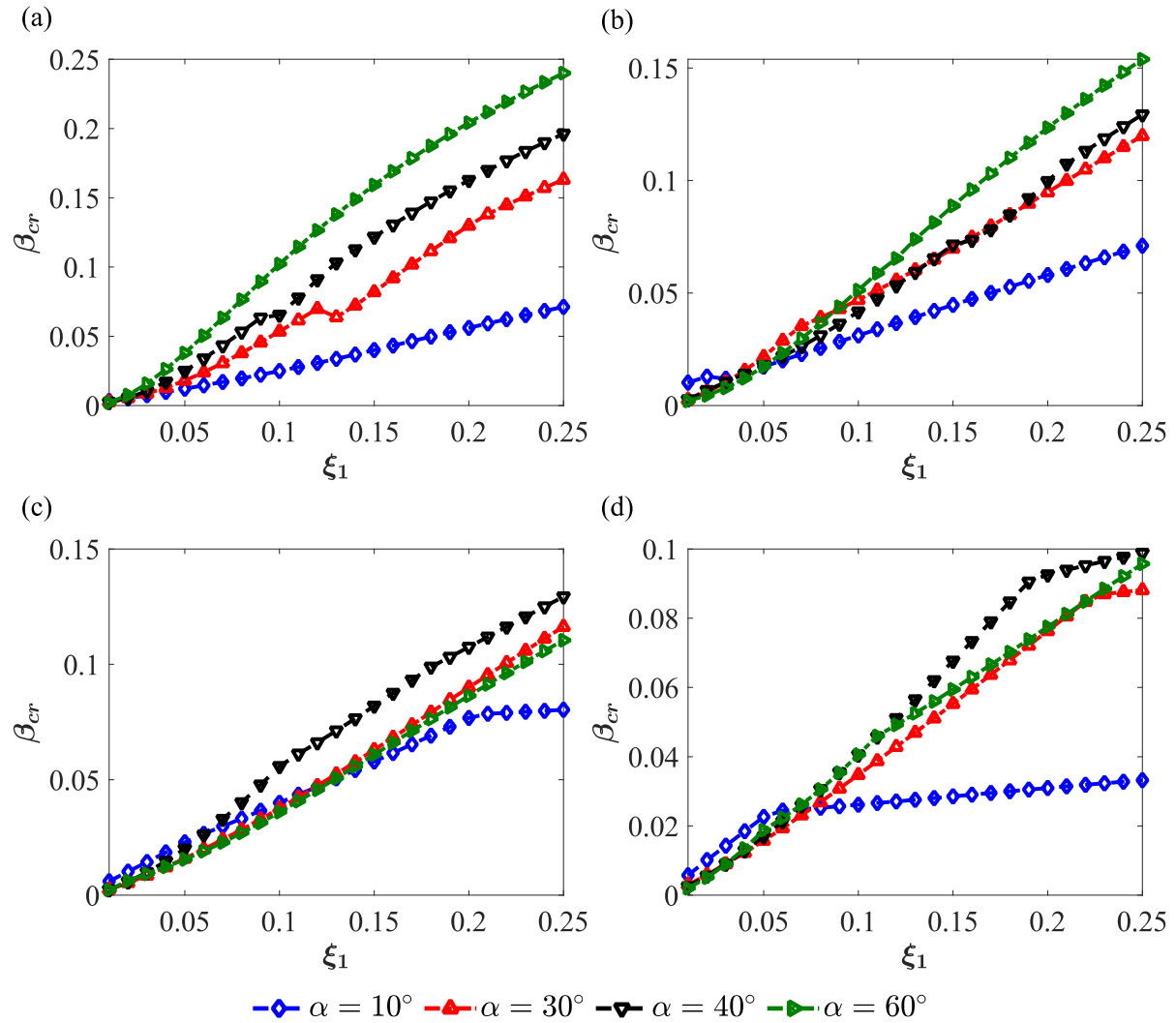


**Fig. D.3.** The non-dimensional critical load ( $\beta_{cr}$ ) of EFGM for different thickness parameter ( $\xi_1$ ), semi-vertex angle ( $\alpha$ ), and slenderness parameter ( $\xi_2$ ) with damping ratio ( $\zeta$ ) = 0.03 : (a)  $\xi_2 = 0.3$ ; (b)  $\xi_2 = 0.5$ ; (c)  $\xi_2 = 0.7$ ; (d)  $\xi_2 = 0.9$ .

## References

- [1] Koizumi M, Niino M. Overview of FGM Research in Japan. MRS Bulletin 1995;20:19–21. <https://doi.org/10.1557/S0883769400048867>.
- [2] Koizumi M. FGM activities in Japan. Composites Part B: Engineering 1997;28:1–4. [https://doi.org/10.1016/S1359-8368\(96\)00016-9](https://doi.org/10.1016/S1359-8368(96)00016-9).
- [3] Udupa G, Rao SS, Gangadharan KV. Functionally Graded Composite Materials: An Overview. Procedia Materials Science 2014;5:1291–9. <https://doi.org/10.1016/j.mspro.2014.07.442>.
- [4] Chi SH, Chung YL. Mechanical behavior of functionally graded material plates under transverse load—Part I: Analysis. International Journal of Solids and Structures 2006;43:3657–74. <https://doi.org/10.1016/J.IJSOLSTR.2005.04.011>.

- [5] Chi S, Chung Y-L. Cracking in coating–substrate composites with multi-layered and FGM coatings. *Engineering Fracture Mechanics* 2003;70:1227–43. [https://doi.org/10.1016/S0013-7944\(02\)00114-5](https://doi.org/10.1016/S0013-7944(02)00114-5).
- [6] Petrolo M, Carrera E. Methods and guidelines for the choice of shell theories. *Acta Mech* 2020;231:395–434. <https://doi.org/10.1007/s00707-019-02601-w>.
- [7] Sofiyev AH. Review of research on the vibration and buckling of the FGM conical shells. *Composite Structures* 2019;211:301–17. <https://doi.org/10.1016/j.compstruct.2018.12.047>.
- [8] Irie T, Yamada G, Kaneko Y. Free vibration of a conical shell with variable thickness. *Journal of Sound and Vibration* 1982;82:83–94. [https://doi.org/10.1016/0022-460X\(82\)90544-2](https://doi.org/10.1016/0022-460X(82)90544-2).
- [9] Irie T, Yamada G, Tanaka K. Natural frequencies of truncated conical shells. *Journal of Sound and Vibration* 1984;92:447–53. [https://doi.org/10.1016/0022-460X\(84\)90391-2](https://doi.org/10.1016/0022-460X(84)90391-2).
- [10] Kayran A, Vinson JR. Free vibration analysis of laminated composite truncated circular conical shells. *AIAA Journal* 1990;28:1259–69. <https://doi.org/10.2514/3.25203>.
- [11] Tong L. Free vibration of composite laminated conical shells. *International Journal of Mechanical Sciences* 1993;35:47–61. [https://doi.org/10.1016/0020-7403\(93\)90064-2](https://doi.org/10.1016/0020-7403(93)90064-2).
- [12] Tong L. Free vibration of laminated conical shells including transverse shear deformation. *International Journal of Solids and Structures* 1994;31:443–56. [https://doi.org/10.1016/0020-7683\(94\)90085-X](https://doi.org/10.1016/0020-7683(94)90085-X).
- [13] Shu C. An efficient approach for free vibration analysis of conical shells. *International Journal of Mechanical Sciences* 1996;38:935–49. [https://doi.org/10.1016/0020-7403\(95\)00096-8](https://doi.org/10.1016/0020-7403(95)00096-8).
- [14] Liew KM, Ng TY, Zhao X. Free vibration analysis of conical shells via the element-free kp-Ritz method. *Journal of Sound and Vibration* 2005;281:627–45. <https://doi.org/10.1016/J.JSV.2004.01.005>.
- [15] Bhangale RK, Ganesan N, Padmanabhan C. Linear thermoelastic buckling and free vibration behavior of functionally graded truncated conical shells. *Journal of Sound and Vibration* 2006;292:341–71. <https://doi.org/10.1016/J.JSV.2005.07.039>.
- [16] Tornabene F, Viola E, Inman DJ. 2-D differential quadrature solution for vibration analysis of functionally graded conical, cylindrical shell and annular plate structures. *Journal of Sound and Vibration* 2009;328:259–90. <https://doi.org/10.1016/J.JSV.2009.07.031>.
- [17] Tornabene F. Free vibration analysis of functionally graded conical, cylindrical shell and annular plate structures with a four-parameter power-law distribution. *Computer Methods in Applied Mechanics and Engineering* 2009;198:2911–35. <https://doi.org/10.1016/j.cma.2009.04.011>.
- [18] Sofiyev AH. Application of the first order shear deformation theory to the solution of free vibration problem for laminated conical shells. *Composite Structures* 2018;188:340–6. <https://doi.org/10.1016/j.compstruct.2018.01.016>.
- [19] Malekzadeh P, Fiouz AR, Sobhrouyan M. Three-dimensional free vibration of functionally graded truncated conical shells subjected to thermal environment. *International Journal of Pressure Vessels and Piping* 2012;89:210–21. <https://doi.org/10.1016/J.IJPVP.2011.11.005>.
- [20] Nejati M, Asanjarani A, Dimitri R, Tornabene F. Static and free vibration analysis of functionally graded conical shells reinforced by carbon nanotubes. *International Journal of Mechanical Sciences* 2017;130:383–98. <https://doi.org/10.1016/j.ijmecsci.2017.06.024>.



- [21] Zghal S, Frikha A, Dammak F. Free vibration analysis of carbon nanotube-reinforced functionally graded composite shell structures. *Applied Mathematical Modelling* 2018;53:132–55. <https://doi.org/10.1016/j.apm.2017.08.021>.
- [22] Sofiyev AH. On the vibration and stability behaviors of heterogeneous- CNTRC-truncated conical shells under axial load in the context of FSDT. *Thin-Walled Structures* 2020;151:106747. <https://doi.org/10.1016/j.tws.2020.106747>.
- [23] Song Z, Cao Q, Dai Q. Free vibration of truncated conical shells with elastic boundary constraints and added mass. *International Journal of Mechanical Sciences* 2019;155:286–94. <https://doi.org/10.1016/j.ijmecsci.2019.02.039>.
- [24] Fares ME, Elmarghany MKh, Atta D, Salem MG. An improved layerwise formulation for free vibrations of multilayered FG truncated conical shells reinforced by carbon nanotubes. *Composite Structures* 2021;275:114372. <https://doi.org/10.1016/j.compstruct.2021.114372>.
- [25] Li H, Hao YX, Zhang W, Liu LT, Yang SW, Wang DM. Vibration analysis of porous metal foam truncated conical shells with general boundary conditions using GDQ. *Composite Structures* 2021;269:114036. <https://doi.org/10.1016/j.compstruct.2021.114036>.
- [26] Zghal S, Trabelsi S, Frikha A, Dammak F. Thermal free vibration analysis of functionally graded plates and panels with an improved finite shell element. *Journal of Thermal Stresses* 2021;44:315–41. <https://doi.org/10.1080/01495739.2021.1871577>.
- [27] Avramov K, Uspensky B, Sakhno N, Nikonov O. Transient response of functionally graded carbon nanotubes reinforced composite conical shell with ring-stiffener under the action of impact loads. *European Journal of Mechanics - A/Solids* 2022;91:104429. <https://doi.org/10.1016/j.euromechsol.2021.104429>.
- [28] Wang J, Wang YQ, Chai Q. Free vibration analysis of a spinning functionally graded spherical–cylindrical–conical shell with general boundary conditions in a thermal environment. *Thin-Walled Structures* 2022;180:109768. <https://doi.org/10.1016/j.tws.2022.109768>.
- [29] Vescovini R, Fantuzzi N. Free vibrations of conical shells via Ritz method. *International Journal of Mechanical Sciences* 2023;241:107925. <https://doi.org/10.1016/j.ijmecsci.2022.107925>.
- [30] Sofiyev AH, Esencan Turkaslan B, Bayramov RP, Salamci MU. Analytical solution of stability of FG-CNTRC conical shells under external pressures. *Thin-Walled Structures* 2019;144:106338. <https://doi.org/10.1016/j.tws.2019.106338>.
- [31] Sofiyev AH. A new approach to solution of stability problem of heterogeneous orthotropic truncated cones with clamped edges within shear deformation theory. *Composite Structures* 2023;304:116411. <https://doi.org/10.1016/j.compstruct.2022.116411>.
- [32] Pakpia J, Aimmanee S, Daud W, Olarnrithinun S. Elasticity and stability of corrugated conical shells with diverse orthotropy. *International Journal of Mechanical Sciences* 2023;108724. <https://doi.org/10.1016/j.ijmecsci.2023.108724>.
- [33] Yang M, Han B, Su P, Zhang Q, Zhang Q, Zhao Z, et al. Crashworthiness of hierarchical truncated conical shells with corrugated cores. *International Journal of Mechanical Sciences* 2021;193:106171. <https://doi.org/10.1016/j.ijmecsci.2020.106171>.
- [34] Sofiyev AH. Influence of the initial imperfection on the non-linear buckling response of FGM truncated conical shells. *International Journal of Mechanical Sciences* 2011;53:753–61. <https://doi.org/10.1016/j.ijmecsci.2011.06.007>.
- [35] Sofiyev AH. Non-linear buckling behavior of FGM truncated conical shells subjected to axial load. *International Journal of Non-Linear Mechanics* 2011;46:711–9. <https://doi.org/10.1016/j.ijnonlinmec.2011.02.003>.

- [36] Sofiyev AH. The non-linear vibration of FGM truncated conical shells. *Composite Structures* 2012;94:2237–45. <https://doi.org/10.1016/J.COMPSTRUCT.2012.02.005>.
- [37] Najafov AM, Sofiyev AH. The non-linear dynamics of FGM truncated conical shells surrounded by an elastic medium. *International Journal of Mechanical Sciences* 2013;66:33–44. <https://doi.org/10.1016/j.ijmecsci.2012.10.006>.
- [38] Sofiyev AH, Kuruoglu N. Non-linear buckling of an FGM truncated conical shell surrounded by an elastic medium. *International Journal of Pressure Vessels and Piping* 2013;107:38–49. <https://doi.org/10.1016/j.ijpvp.2013.03.010>.
- [39] Deniz A, Sofiyev AH. The nonlinear dynamic buckling response of functionally graded truncated conical shells. *Journal of Sound and Vibration* 2013;332:978–92. <https://doi.org/10.1016/j.jsv.2012.09.032>.
- [40] Sofiyev AH. Parametric vibration of FGM conical shells under periodic lateral pressure within the shear deformation theory. *Composites Part B: Engineering* 2016;89:282–94. <https://doi.org/10.1016/j.compositesb.2015.11.017>.
- [41] Najafov AM, Sofiyev AH, Kuruoglu N. On the solution of nonlinear vibration of truncated conical shells covered by functionally graded coatings. *Acta Mech* 2014;225:563–80. <https://doi.org/10.1007/s00707-013-0980-5>.
- [42] Zghal S, Frikha A, Dammak F. Mechanical buckling analysis of functionally graded power-based and carbon nanotubes-reinforced composite plates and curved panels. *Composites Part B: Engineering* 2018;150:165–83. <https://doi.org/10.1016/j.compositesb.2018.05.037>.
- [43] Trabelsi S, Frikha A, Zghal S, Dammak F. Thermal post-buckling analysis of functionally graded material structures using a modified FSDT. *International Journal of Mechanical Sciences* 2018;144:74–89. <https://doi.org/10.1016/j.ijmecsci.2018.05.033>.
- [44] Trabelsi S, Frikha A, Zghal S, Dammak F. A modified FSDT-based four nodes finite shell element for thermal buckling analysis of functionally graded plates and cylindrical shells. *Engineering Structures* 2019;178:444–59. <https://doi.org/10.1016/j.engstruct.2018.10.047>.
- [45] Trabelsi S, Zghal S, Dammak F. Thermo-elastic buckling and post-buckling analysis of functionally graded thin plate and shell structures. *J Braz Soc Mech Sci Eng* 2020;42:233. <https://doi.org/10.1007/s40430-020-02314-5>.
- [46] Allahkarami F, Ghassabzadeh Saryazdi M, Tohidi H. Dynamic buckling analysis of bi-directional functionally graded porous truncated conical shell with different boundary conditions. *Composite Structures* 2020;252:112680. <https://doi.org/10.1016/j.compstruct.2020.112680>.
- [47] Zarei M, Rahimi GH, Hemmatnezhad M. Global buckling analysis of laminated sandwich conical shells with reinforced lattice cores based on the first-order shear deformation theory. *International Journal of Mechanical Sciences* 2020;187:105872. <https://doi.org/10.1016/j.ijmecsci.2020.105872>.
- [48] Fu T, Wu X, Xiao Z, Chen Z. Study on dynamic instability characteristics of functionally graded material sandwich conical shells with arbitrary boundary conditions. *Mechanical Systems and Signal Processing* 2021;151:107438. <https://doi.org/10.1016/j.ymssp.2020.107438>.
- [49] Zghal S, Trabelsi S, Dammak F. Post-buckling behavior of functionally graded and carbon-nanotubes based structures with different mechanical loadings. *Mechanics Based Design of Structures and Machines* 2022;50:2997–3039. <https://doi.org/10.1080/15397734.2020.1790387>.
- [50] Zghal S, Dammak F. Vibration characteristics of plates and shells with functionally graded pores imperfections using an enhanced finite shell element. *Computers &*

- [51] Huang X, Wang J, Wei N, Wang C, Ma B. Buckling and vibration of porous sigmoid functionally graded conical shells. *Journal of Theoretical and Applied Mechanics* 2023;61:559–71. <https://doi.org/10.15632/jtam-pl/168072>.
- [52] Hasan HM, Alkhfaji SS, Mutlag SA. Torsional postbuckling characteristics of functionally graded graphene enhanced laminated truncated conical shell with temperature dependent material properties. *Theoretical and Applied Mechanics Letters* 2023;13:100453. <https://doi.org/10.1016/j.taml.2023.100453>.
- [53] Ibrahim HH, Tawfik M, Al-Ajmi M. Non-linear panel flutter for temperature-dependent functionally graded material panels. *Computational Mechanics* 2008;41:325–34. <https://doi.org/10.1007/s00466-007-0188-4>.
- [54] Ibrahim HH, Yoo HH, Lee K-S. Supersonic Flutter of Functionally Graded Panels Subject to Acoustic and Thermal Loads. *Journal of Aircraft* 2009;46:593–600. <https://doi.org/10.2514/1.39085>.
- [55] Mahmoudkhani S, Haddadpour H, Navazi HM. Supersonic flutter prediction of functionally graded conical shells. *Composite Structures* 2010;92:377–86. <https://doi.org/10.1016/J.COMPSTRUCT.2009.08.018>.
- [56] Sabri F, Lakis AA. Efficient Hybrid Finite Element Method for Flutter Prediction of Functionally Graded Cylindrical Shells. *Journal of Vibration and Acoustics* 2013;136. <https://doi.org/10.1115/1.4025397>.
- [57] Su Z, Wang L, Sun K, Wang D. Vibration characteristic and flutter analysis of elastically restrained stiffened functionally graded plates in thermal environment. *International Journal of Mechanical Sciences* 2019;157–158:872–84. <https://doi.org/10.1016/J.IJMECSCI.2019.05.028>.
- [58] Wei J, Song Z, Li F. Superior aeroelastic behaviors of axially functional graded cylindrical shells in supersonic airflow. *Journal of Fluids and Structures* 2020;96:103027. <https://doi.org/10.1016/J.JFLUIDSTRUCTS.2020.103027>.
- [59] Sun Y, Song Z, Ma W, Li F. Influence mechanism of lumped masses on the flutter behavior of structures. *Aerospace Science and Technology* 2021;111:106524. <https://doi.org/10.1016/J.AST.2021.106524>.
- [60] Muc A, Flis J. Flutter characteristics and free vibrations of rectangular functionally graded porous plates. *Composite Structures* 2021;261:113301. <https://doi.org/10.1016/J.COMPSTRUCT.2020.113301>.
- [61] Zhou X, Wang Y, Zhang W. Vibration and flutter characteristics of GPL-reinforced functionally graded porous cylindrical panels subjected to supersonic flow. *Acta Astronautica* 2021;183:89–100. <https://doi.org/10.1016/J.ACTAASTRO.2021.03.003>.
- [62] AminYazdi A. Flutter of geometrical imperfect functionally graded carbon nanotubes doubly curved shells. *Thin-Walled Structures* 2021;164:107798. <https://doi.org/10.1016/j.tws.2021.107798>.
- [63] Avramov K, Uspensky B. Nonlinear supersonic flutter of sandwich truncated conical shell with flexible honeycomb core manufactured by fused deposition modeling. *International Journal of Non-Linear Mechanics* 2022;143:104039. <https://doi.org/10.1016/j.ijnonlinmec.2022.104039>.
- [64] Houshang A, Jafari AA, Haghighi SE, Nezami M. Supersonic flutter characteristics of truncated sandwich conical shells with MR core. *Thin-Walled Structures* 2022;173:108888. <https://doi.org/10.1016/j.tws.2022.108888>.
- [65] Banijamali SM, Jafari AA. Vibration analysis and critical speeds of a rotating functionally graded conical shell stiffened with Anisogrid lattice structure based on

- FSDT. Thin-Walled Structures 2023;188:110841. <https://doi.org/10.1016/j.tws.2023.110841>.
- [66] Kumar A, Ray MC. Control of smart rotating laminated composite truncated conical shell using ACLD treatment. *International Journal of Mechanical Sciences* 2014;89:123–41. <https://doi.org/10.1016/j.ijmecsci.2014.08.026>.
- [67] Tsushima N, Su W. Flutter suppression for highly flexible wings using passive and active piezoelectric effects. *Aerospace Science and Technology* 2017;65:78–89. <https://doi.org/10.1016/j.ast.2017.02.013>.
- [68] Zhang LW, Song ZG, Liew KM. Modeling aerothermoelastic properties and active flutter control of nanocomposite cylindrical shells in supersonic airflow under thermal environments. *Computer Methods in Applied Mechanics and Engineering* 2017;325:416–33. <https://doi.org/10.1016/j.cma.2017.07.014>.
- [69] Song Z-G, Yang T-Z, Li F-M, Carrera E, Hagedorn P. A Method of Panel Flutter Suppression and Elimination for Aeroelastic Structures in Supersonic Airflow. *Journal of Vibration and Acoustics* 2018;140. <https://doi.org/10.1115/1.4039724>.
- [70] Langthjem MA, Sugiyama Y. Dynamic stability of columns subjected to follower loads: A survey. *Journal of Sound and Vibration* 2000;238:809–51. <https://doi.org/10.1006/JSVI.2000.3137>.
- [71] Elishakoff I. Controversy Associated With the So-Called “Follower Forces”: Critical Overview. *Applied Mechanics Reviews* 2005;58:117–42. <https://doi.org/10.1115/1.1849170>.
- [72] Park SH, Kim JH. Dynamic stability of a completely free circular cylindrical shell subjected to a follower force. *Journal of Sound and Vibration* 2000;231:989–1005. <https://doi.org/10.1006/JSVI.1999.2319>.
- [73] Torki ME, Kazemi MT, Haddadpour H, Mahmoudkhani S. Dynamic stability of cantilevered functionally graded cylindrical shells under axial follower forces. *Thin-Walled Structures* 2014;79:138–46. <https://doi.org/10.1016/J.TWS.2013.12.005>.
- [74] Torki ME, Kazemi MT, Reddy JN, Haddadpoud H, Mahmoudkhani S. Dynamic stability of functionally graded cantilever cylindrical shells under distributed axial follower forces. *Journal of Sound and Vibration* 2014;333:801–17. <https://doi.org/10.1016/J.JSV.2013.09.005>.
- [75] Robinson MTA, Adali S. Nonconservative stability of viscoelastic rectangular plates with free edges under uniformly distributed follower force. *International Journal of Mechanical Sciences* 2016;107:150–9. <https://doi.org/10.1016/j.ijmecsci.2015.12.029>.
- [76] Mardanpour P, Izadpanahi E, Rastkar S, Fazelzadeh SA, Hodges DH. Geometrically Exact, Fully Intrinsic Analysis of Pre-Twisted Beams Under Distributed Follower Forces. *AIAA Journal* 2018;56:836–48. <https://doi.org/10.2514/1.J055744>.
- [77] Izadpanahi E, Rastkar S, Zisis I, Fazelzadeh SA, Mardanpour P. Nonlinear time domain and stability analysis of beams under partially distributed follower force. *Applied Mathematical Modelling* 2019;73:303–26. <https://doi.org/10.1016/j.apm.2019.04.031>.
- [78] Ventura P, Azzayani H, Zahrouni H, Potier-Ferry M. Buckling of pressurized cylindrical shells using the Asymptotic Numerical Method. *Thin-Walled Structures* 2023;188:110835. <https://doi.org/10.1016/j.tws.2023.110835>.
- [79] Do V-D, Le Grogne P, Rohart P. Closed-form solutions for the elastic–plastic buckling design of shell structures under external pressure. *European Journal of Mechanics - A/Solids* 2023;98:104861. <https://doi.org/10.1016/j.euromechsol.2022.104861>.
- [80] Mazidi A, Fazelzadeh SA, Marzocca P. Flutter of Aircraft Wings Carrying a Powered Engine Under Roll Maneuver. *Journal of Aircraft* 2011;48:874–83. <https://doi.org/10.2514/1.C031080>.

- [81] Fazlzadeh SA, Mazidi A. Nonlinear aeroelastic analysis of bending-torsion wings subjected to a transverse follower force. *Journal of Computational and Nonlinear Dynamics* 2011;6. <https://doi.org/10.1115/1.4003288>.
- [82] Mazidi A, Kalantari H, Fazlzadeh SA. Aeroelastic response of an aircraft wing with mounted engine subjected to time-dependent thrust. *Journal of Fluids and Structures* 2013;39:292–305. <https://doi.org/10.1016/j.jfluidstructs.2013.02.024>.
- [83] Reddy JN. Analysis of functionally graded plates. *International Journal for Numerical Methods in Engineering* 2000;47:663–84. [https://doi.org/10.1002/\(SICI\)1097-0207\(20000110/30\)47:1/3<663::AID-NME787>3.0.CO;2-8](https://doi.org/10.1002/(SICI)1097-0207(20000110/30)47:1/3<663::AID-NME787>3.0.CO;2-8).
- [84] Kim JH, Kim HS. A study on the dynamic stability of plates under a follower force. *Computers & Structures* 2000;74:351–63. [https://doi.org/10.1016/S0045-7949\(99\)00023-1](https://doi.org/10.1016/S0045-7949(99)00023-1).
- [85] Jung WY, Han SC. Transient analysis of FGM and laminated composite structures using a refined 8-node ANS shell element. *Composites Part B: Engineering* 2014;56:372–83. <https://doi.org/10.1016/J.COMPOSITESB.2013.08.044>.
- [86] Barsoum RS. Finite element method applied to the problem of stability of a non-conservative system. *International Journal for Numerical Methods in Engineering* 1971;3:63–87. <https://doi.org/10.1002/nme.1620030110>.
- [87] Zhao X, Liew KM. Free vibration analysis of functionally graded conical shell panels by a meshless method. *Composite Structures* 2011;93:649–64. <https://doi.org/10.1016/J.COMPSTRUCT.2010.08.014>.